

Sensing environmental interaction physics to traverse cluttered obstacles

Yaqing Wang, Ling Xu, Chen Li*

Department of Mechanical Engineering, Johns Hopkins University

Corresponding author: chen.li@jhu.edu

Abstract

When legged robots physically interact with obstacles in applications such as search and rescue through rubble and planetary exploration across Martian rocks, even the most advanced ones struggle because they lack a fundamental framework to model the robot-obstacle physical interaction paralleling artificial potential fields for obstacle avoidance. To remedy this, recent studies established a novel framework—potential energy landscape modeling—that explains and predicts the destabilizing transitions across locomotor modes from the physical interaction between robots and obstacles, and governs a wide range of complex locomotion. However, this framework was confined to the laboratory because we lack methods to obtain the potential energy landscape in unknown environments. Here, we explore the feasibility of introducing this framework to such environments. We showed that a robot can reconstruct the potential energy landscape for unknown obstacles by measuring the obstacle contact forces and resulting torques. To elaborate, we developed a minimalistic robot capable of sensing contact forces and torques when propelled against a pair of grass-like obstacles. Despite the forces and torques not being fully conservative, they well-matched the potential energy landscape gradients, and the reconstructed landscape well-matched ground truth. In addition, we found that using normal forces and torques and head oscillation inspired by cockroach observations further improved the estimation of conservative ones. Our study will finally inspire free-running robots to achieve low-effort, “zero-shot” traversing clustered, large obstacles in real-world applications by sampling contact forces and torques and reconstructing the landscape around its neighboring states in real time.

INTRODUCTION

Sensing one's surrounding environment helps animals and robots move through the complex world. Animals (including humans) combine vision and other sensory modalities (mechanosensing like tactile and proprioception, chemosensing, etc.) to sense, plan, and control their interaction with obstacles to *traverse* them (1–3). By contrast, robots heavily rely on visual information to navigate complex environments while *avoiding* obstacles (4) (**Fig. 1**, top row). Specifically, a robot often uses long-ranged visual sensing (e.g., cameras, LiDAR) (e.g., **Fig. 1A**) to create a geometric map of the environment (e.g., **Fig. 1B**). Using this map, it constructs an artificial potential field (5, 6), with its goal modeled by a global minimum and obstacles modeled by high potential regions. It then plans and follows a gradient descent path towards the goal while avoiding the obstacles (7) (**Fig. 1C**), often transitioning between various locomotor modes (e.g., **Fig. 1D**).

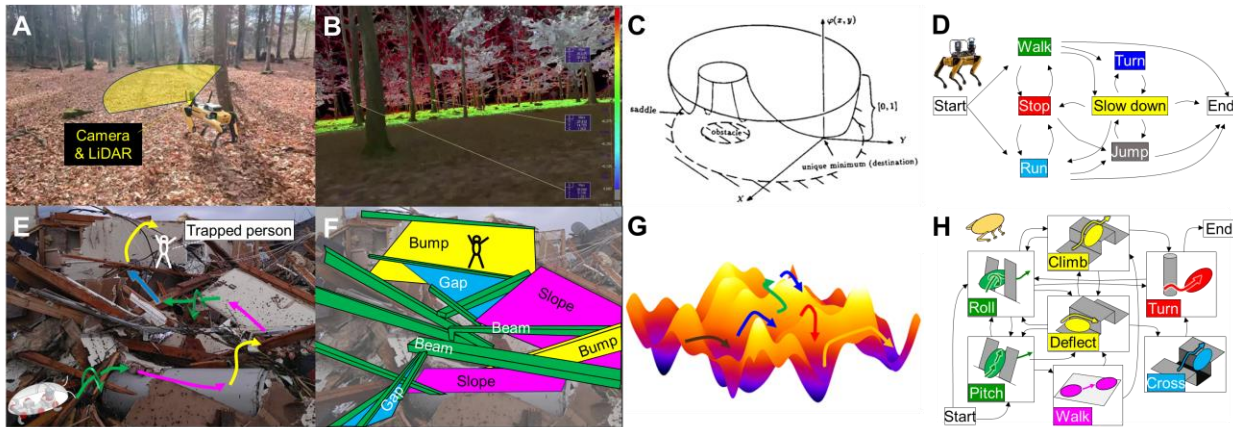


Fig. 1. Envisioned potential energy landscape approach enabling legged obstacle traversal analogous to artificial potential field enables obstacle avoidance. (A) A legged robot leverages vision-based sensory to navigate a flat, sparse forest terrain with scattered trees. (B) Geometric map scanned using LiDAR from the robot in (A). (C) Artificial potential field approach for obstacle avoidance. (D) Multi-pathway driving transitions to avoid obstacles. (E) Envisioned traversal of cluttered large obstacles to be enabled (e.g., earthquake rubble for search and rescue). (F) Identified locomotor challenges from large, diverse obstacles, whose environmental interaction physics needs to be sensed to enable robust traversal. (G) Potential energy

landscape approach for obstacle traversal. **(H)** Multi-pathway locomotor transitions to traverse via sensing and controlling physical interaction with obstacles. **(B)** is adapted from (8). **(C)** is adapted from (5). **(E, G)** is adapted from (9). **(H)** is adapted from (10).

However, this vision-based approach of robot navigation fails in environments with densely cluttered (spacing \sim body size), large (\sim body size) obstacles, where a collision-free trajectory to the goal simply may not exist. Instead, a robot must physically interact with obstacles and/to generate appropriate forces and torques. However, a lack of sensing physical interaction with obstacles leads to poor control of locomotion through them. Also, the artificial potential field for avoidance cannot plan effective paths for robots to physically interact with obstacles to traverse. These challenges have diminished the usefulness of robots in many important applications, such as search and rescue in rubble (11) (**Fig. 1E**), environmental monitoring in mountain boulders and forest debris (12), and planetary exploration through large Martian and Lunar rocks (13).

To traverse densely cluttered terrains, a robot must sense not only environmental geometry but also physical interaction, so that it can control its self-propulsion to generate appropriate forces and torques to overcome obstacles, planning and following small-resistant paths guided by environmental models that take into account physical interaction as well as geometry (9, 10). Towards this vision, our lab recently established a new approach to modeling environmental interaction, using potential energy landscapes resulting from the physical interaction of robots (and animals) (**Fig. 1**, bottom) with a diversity of large obstacles that present distinct locomotor challenges (e.g., **Fig. 1F**) (9, 10, 14–18). Analogous to artificial potential fields for geometry-based obstacle avoidance, these real potential energy landscapes (**Fig. 1G**) provide a physics-based foundation for robots to conceptualize locomotor transitions (**Fig. 1H**) to traverse (for a review, see (10)).

Specifically, a self-propelled robot's (or animal's) body physically interacts with obstacles, resulting in a potential energy landscape (the system's real potential energy as a function of body 3-D position and rotation), with attractive basins of stability separated by potential energy barriers (**Fig. 1G**). Due to continual self-propulsion breaking continuous frictional contacts, the system's state tends to settle

to these basins. As the robot (or animal) is attracted to each stability basin on the landscape, its motion emerges as a distinct locomotor mode (which often involves large body rotations, not just translation) (**Fig. 1H**). Given the limited propulsive forces and torques of the robot (or animal), some modes can lead to traversal, while others lead to being trapped. Thus, to traverse, the robot (or animal) must propel to destabilize itself from attraction by the basins/modes of entrapment and overcome potential energy barriers to transition to the basins/modes that lead to traversal. Because these barrier-crossing transitions are highly strenuous (requiring the generation of large propulsion and work compared to the robot's (or animal's) capacity), it is beneficial to sense the potential energy landscape, find saddles (lowest points) on the barriers, and cross the barriers via saddles, as doing so has the least resistance and requires the least effort (*10*).

Our lab's recent simulation study supports the usefulness of obstacle contact force and torque sensing in real robots (*19*). By sensing the total obstacle interaction force from a known type of obstacle, a simulation robot can escape from entrapment in a more strenuous locomotor mode and transition to a less strenuous mode, thereby traversing with less effort or even enabling traversal given limited propulsion.

Given these advances in modeling environmental physical interaction in densely cluttered terrains using potential energy landscapes, as well as simulation evidence of the usefulness of sensing physical interaction, how to sense the potential energy landscape is unsolved. A system's potential energy landscape gradients are the conservative forces and torques, so, to sense the potential energy landscape, the robot must sense forces and torques. However, obstacle contact forces and torques also have contributions from non-conservative forces (frictional forces, damping forces, inertial forces, etc.) and torques. Yet, our lab's previous works demonstrated that the system's locomotor mode transition dynamics are strongly governed by the potential energy landscape in densely cluttered terrains (*10*). This suggests that the conservative forces and torques (landscape gradients) dominate, and the non-conservative forces and torques are small. In other words, the total contact forces and torques should well approximate the conservative forces and torques. Thus, we hypothesized that the potential energy landscape can be reconstructed from obstacle contact forces and torques.

Testing our hypothesis requires us to create a robot with custom onboard sensors to measure obstacle contact forces and torques on its body. Many robots already equipped one force/torque sensor in each leg to sense foot–ground interaction (20, 21), which may help stabilize upright running and walking on the ground with small unevenness (\ll leg length) (22–24). However, traversing cluttered large obstacles (i.e., terrain unevenness \sim leg length) requires sensing the more general body–environment interaction. Because, to traverse densely cluttered terrain, the robot transitions across locomotor modes with large body rotations, changing where the body contacts obstacles. To sense every contact, multiple sensors distributed over the body are required. Moreover, self-propulsion during interacting with cluttered large obstacles always induces continual collisions with the obstacles (10), where sophisticated commercial sensors capable of measuring both forces and torques (e.g., ATI F/T sensors, OnRobot HEX-E series, FUTEK LCF series) are too fragile for this purpose (and too expensive to have multiple ones). Recent studies began to address this problem by developing flexible sensory arrays (25–30). However, these sensors only provide 1-D force (normal force) sensation, have long sensory cycles (for sequentially measuring a voltage on each cell), have obvious dead zones and delay, and require substantial effort and special equipment to manufacture. All these challenges encouraged us to develop new custom sensors and sensing strategies.

Here, we take the next step towards our vision by creating a robot equipped with custom distributed force and contact sensors on its body for sensing obstacle contact forces and torques, and using the robot to test how well the potential energy landscape can be estimated from the sensed forces and torques. Specifically, the robot senses contact force and position with each obstacle from two kinds of custom sensors, and calculates the resulting torque. We controlled the robot to traverse cluttered obstacles with prescribed trajectories over a broad range of relevant states (including both transitions and rotations) while sensing forces and torques, and tested how well the sensed obstacle contact forces and torques matched the landscape gradients and how well the potential energy landscape was estimated. We also tested whether using normal forces (i.e., eliminating friction) and torques improved the landscape gradient estimation.

Attempting to further improve the landscape gradient estimation, we considered robotic active sensing behavior. It is well-known that many animals use active sensing behavior when physically

interacting with obstacles (18, 31). However, the mechanics of how this modulates the sensed signal and benefits obstacle estimation are not fully understood. To begin to understand animal behavior and learn how to apply this to robots, we controlled the robot to make a feedforward motion similar to a prospective active sensing motion observed from an animal, and tested how this modulates the sensed forces and torques.

RESULTS

Model system

Our study focuses on the model system of grass-like beam obstacle traversal, building on our lab's previous works (9, 14, 18) (**Fig. 2A, B**). To traverse relatively stiff, cluttered beam obstacles with gaps narrower than its body width, the discoid cockroach or a cockroach-inspired robot often transitions from a strenuous pitch mode (pushing forward across beams with large body pitching), which requires a large propulsive force and mechanical energy cost (**Fig. 2A, B**, blue), to a much easier roll mode (rolling into beam gaps and maneuvering through), which requires a much smaller propulsion and mechanical energy cost (**Fig. 2A, B**, red). When the trajectory of the system (**Fig. 2C**) is viewed on the potential energy landscape over the animal's or robot's body roll-pitch space (**Fig. 2D**), this pitch-to-roll transition (**Fig. 2C, iii'**) requires escaping the entrapment in a pitch basin (**Fig. 2D, ii, iii**, blue), crossing a potential energy barrier, and reaching a roll basin (**Fig. 2D, ii, iii**, red). These basins emerge and morph as the body moves forward, changing the pitch-to-roll transition potential energy barrier (**Fig. 2D, ii, iii**, gray dashed curve).

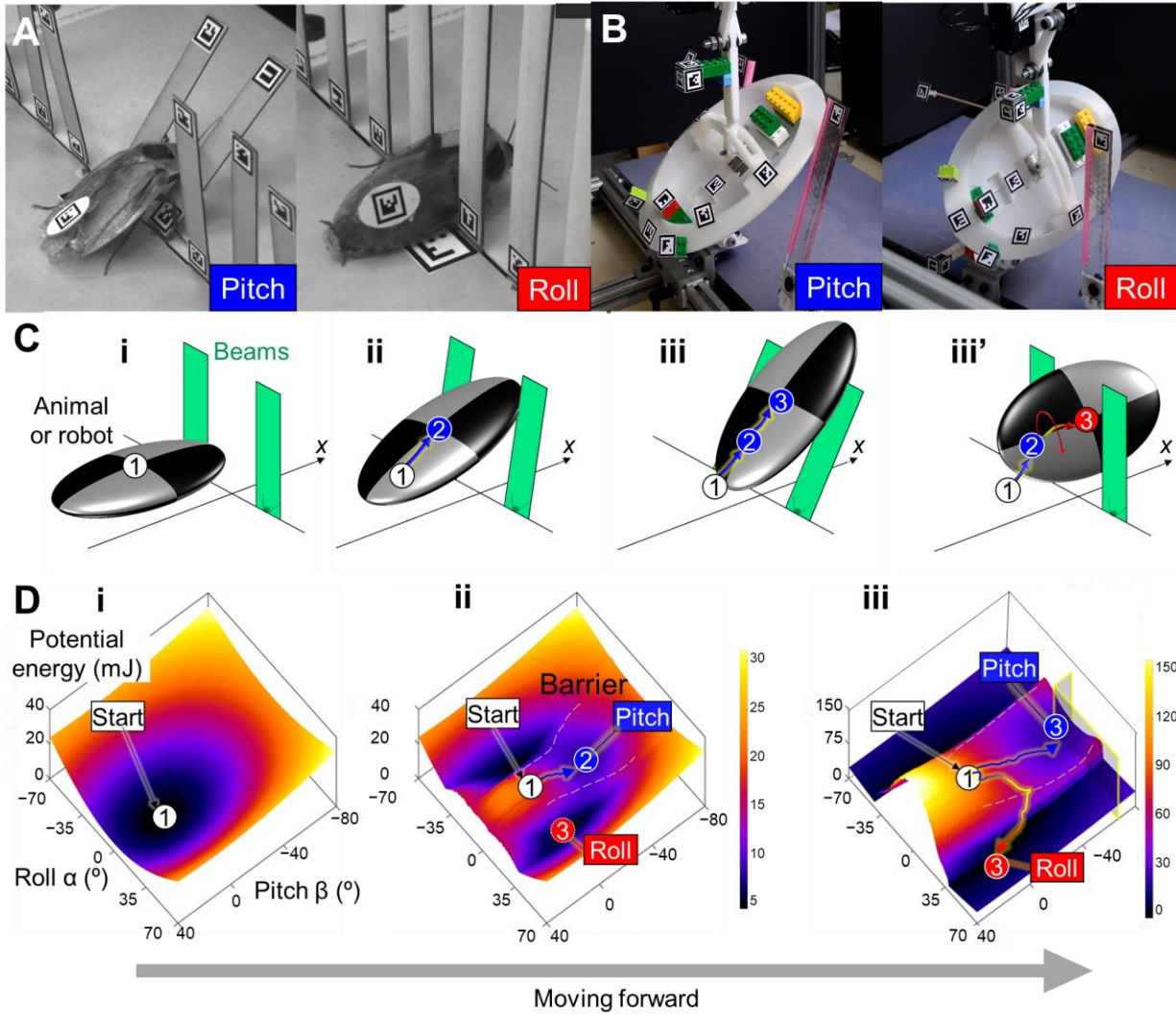


Fig. 2. Model system of cluttered beam obstacle traversal. (A, B) When (A) a cockroach and (B) a minimalistic, feedforward robot traverse cluttered grass-like beams with small gaps ($<$ body width), they either use a strenuous pitch mode to push across (left, blue) or a less strenuous roll mode, where after rolling they maneuver through the gap (right, red) (9). (C) Schematics of animal or robot's body interacting with two beams. The body was an ellipsoid (checkered). The beams were rigid rectangle plates (green) attached to the ground with torsional springs at the bottom. After coming close to the beams (i), the body interacts with beams either using the pitch mode (ii, iii) or transitioning to the roll mode (iii'). (D) Snapshots of the potential energy landscape over roll-pitch (α - β) space. Before physically interacting with the beams (i), the landscape has a global basin. During interaction (ii, iii), a pitch basin and left- and right-roll basins emerge

on the landscape, separated by potential energy barriers (gray dashed curves). The start (running), pitch, or roll locomotor mode (white, blue, or red circles in (C)) emerges as the system is attracted to the global, pitch, or roll basin (white, blue, or red circle in (D)), separately. Arrows on the landscape show examples of state trajectory. Figure adapted from (9).

New robot capable of obstacle contact force and torque sensing

To systematically study obstacle contact force and torque sensing and landscape reconstruction, we iteratively developed (**Fig. S4**) a minimalistic, cockroach-inspired robot (**Fig. 3**) with the ability to sense contact forces and torques while moving forward at a constant speed, with prescribed body roll and pitch that was varied across trials.

Our robotic system is upgraded from the previous sensor-less robot for studying the passive dynamics of the system (9), consisting of a robot with an outer shape similar to the discoid cockroach traversing a pair of deflectable beams (**Fig. 3A**), mimicking the cockroach traverses grass-like obstacles. Upon the previous design, the robot was further cropped from a full shape (**Fig. 3B**, translucent green) to only keep the regions that contact the beams. To sense contact forces and torques, we separated the robot into body and shells, added customized 3-D force sensors between the body and shells (**Fig. 3B**, magenta), and added contact sensors to the shell surface (**Fig. 3B**, yellow and orange). The body was driven forward (**Fig. 3A**, white) by an external translational motor (**Fig. 3B**, black) to emulate the forward propulsion generated by legs, but without adding legs. For systematically measuring obstacle contact forces and torques over a broad range of roll and pitch, which are needed to reconstruct the potential energy landscape, we added two motors (**Fig. 3B**, red and blue) that rigidly attached to the robot rotational axes (**Fig. 3A**, red and blue), to prescribe body roll and pitch.

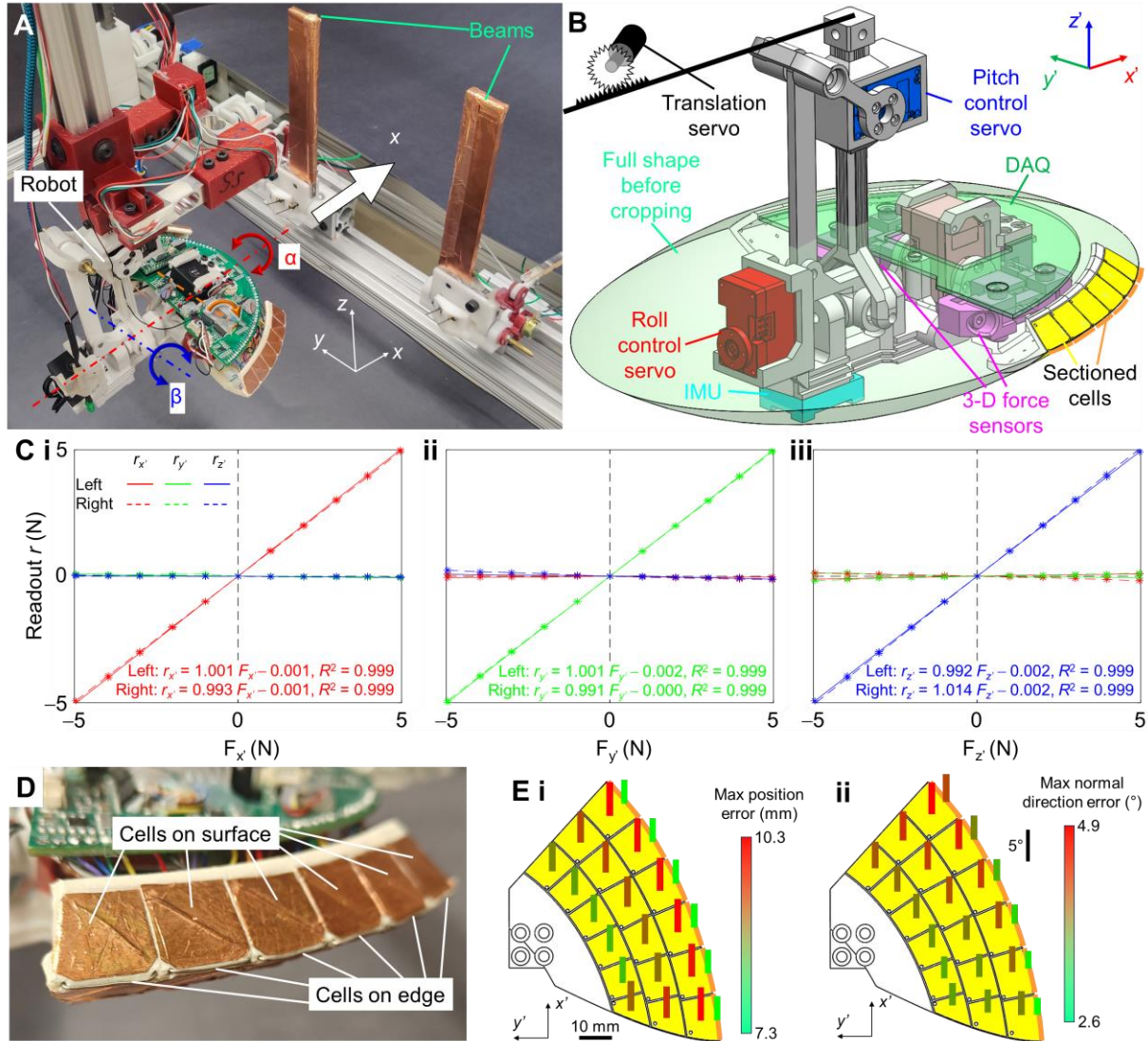


Fig. 3. New robotic system for sensing obstacle contact forces and torques. (A) Photo of the system consisting of a robot with force and contact sensors and two beams. x , y , and z axes show the lab frame. White, red, and blue arrows show translation in fore-aft (x), and rotation in roll (α) and pitch (β) directions, separately. (B) CAD model of the robot. The shells were cropped from a full shape (translucent green). The robot is propelled forward along $+x$ direction at a constant speed (white arrow in (A)) by a servo motor via gear-rack mechanism (black). Body roll and pitch (red and blue arrows in (A)) are controlled by servo motors (red and blue). To sense contact forces and torques on the body, 3-D force sensors (magenta) and touch sensory cells (yellow and orange) are added. To verify the robot rotation, an inertial measurement unit (IMU, cyan) is added. x' -, y' -, and z' - axes show the robot body frame. (C) Custom 3-D force sensor

calibration. Curves show the sensor readout r (red: x' , green: y' , blue: z') as a function of applied force F in body (i) x' -, (ii) y' -, and (iii) z' - axes, separately. Solid and dashed curves are from the left and right sensors, separately. It is hard to differentiate the left and right curves, because the two sensors are highly identical. Formula shows linear regression results between sensor readout r and applied force F in the same axes, which all show high linearity ($R^2 = 0.999$). **(D)** Touch sensory cells on the surface and edge, detecting contact positions. They enable contact torque calculation when combined with force sensing. **(E)** Maximum (i) position and (ii) normal direction error on each touch-sensitive cell. The pattern of cells is from robot bottom view. x' - and y' -axes show robot body frame. Because the left and right shells are mirrored, only the right shell is shown. Because the cells above the edge are mirrored from those beneath the edge, only the bottom cells are shown. Bar rooting at the center of a cell shows error on that cell, whose height and color shows error magnitude. With a careful cell pattern design, the maximum position and normal direction errors are small and roughly constant across the shell surface.

Contact force and torque sensor design and calibration

To sense obstacle contact forces and torques, we added force and contact sensors to the robot. Specifically, to measure the contact force with either beam, the robot's outer shell was separated into left and right parts. We connected each piece of shell with the body frame via a custom small (58 mm \times 44 mm \times 22 mm), low-cost 3-axis force sensor (**Fig. 3B**, magenta), each consisting of three load cells serially connected and orthogonal to one other. Each load cell provided a separate force measurement along the robot body x' -, y' -, or z' -axis, with a labeled range of ± 20 N and precision of ± 0.004 N, which suited our experiment where the contact forces were < 10 N. A force calibration (**Fig. 3C**) shows that both left and right custom force sensors have high linearity between their readouts and applied forces in the same body frame axes ($R^2 = 0.999$) and small crosstalk between their readouts and applied forces in different axes ($< 4\%$). See Section **S4** for force sensor calibration method. To get contact torque, we detected the contact position with each beam by attaching sectioned touch-sensitive cells (**Fig. 3D**) made of copper tape (32) on the shell surface (**Fig. 3B**, yellow) and metal wires (0.5 mm in diameter) on the shell edge (**Fig. 3B**, orange),

and calculated the contact torque combining the contact force and position data. The pattern of the touch sensory cell distribution was carefully designed so that the measurement resolutions of contact position and normal direction were within small thresholds (i.e., position resolution < 11 mm, normal direction resolution $< 5^\circ$, see Section *Force analyses and accuracy optimization* in *Materials and Methods* for definitions) (**Fig. 3E**), which is achieved by gradually revising touch sensor pattern design in the iterative development process (**Fig. S4**).

Trends of contact forces and torques matched with the landscape gradients

To estimate the potential energy landscape over the state space (x - α - β , corresponding to fore-aft position, roll, and pitch angles) in the model system of beam traversal, we let the robot systematically vary the fore-aft position and roll and pitch angles. Before each trial, the roll and pitch angles were set to the desired values, and then the body was driven forward to traverse the beam obstacles, while the force sensors recorded the 3-D contact forces (**Fig. 4A**, red) and the contact sensors recorded the contact positions with each beam on the body (**Fig. 4A**, orange) at 50 Hz. Contact roll and pitch torques from each beam were calculated based on contact forces and positions (see Section *Force analyses and accuracy optimization* in *Materials and Methods*).

We observed several trends of the measured forces and torques (**Fig. 4B, C**) in the x - α - β space, namely, the fore-aft force F_x , roll torque T_α , and pitch torque T_β . (1) The fore-aft force was always negative (averaged $F_x = -2.0 \pm 0.4$ N) when the robot contacted the beams. (2) For a small roll angle ($\alpha = 0^\circ - 30^\circ$), the roll torque was near-zero (averaged $T_\alpha = 7 \pm 17$ N·mm). (3) For a large roll angle ($\alpha = 35^\circ - 40^\circ$), the roll torque was positive (maximum $T_\alpha = 98 \pm 66$ N·mm) at first, but then suddenly reduced to negative (minimum $T_\alpha = -41 \pm 45$ N·mm). (4) For a small pitch angle ($|\beta| = 10^\circ - 20^\circ$), the pitch torque was positive (maximum $T_\beta = 27 \pm 22$ N·mm) at first, but then reduced to negative (minimum $T_\beta = -98 \pm 46$ N·mm). (5) For a large pitch angle ($|\beta| = 25^\circ - 40^\circ$), the pitch torque was always negative (averaged $T_\beta = -45 \pm 20$ N·mm).

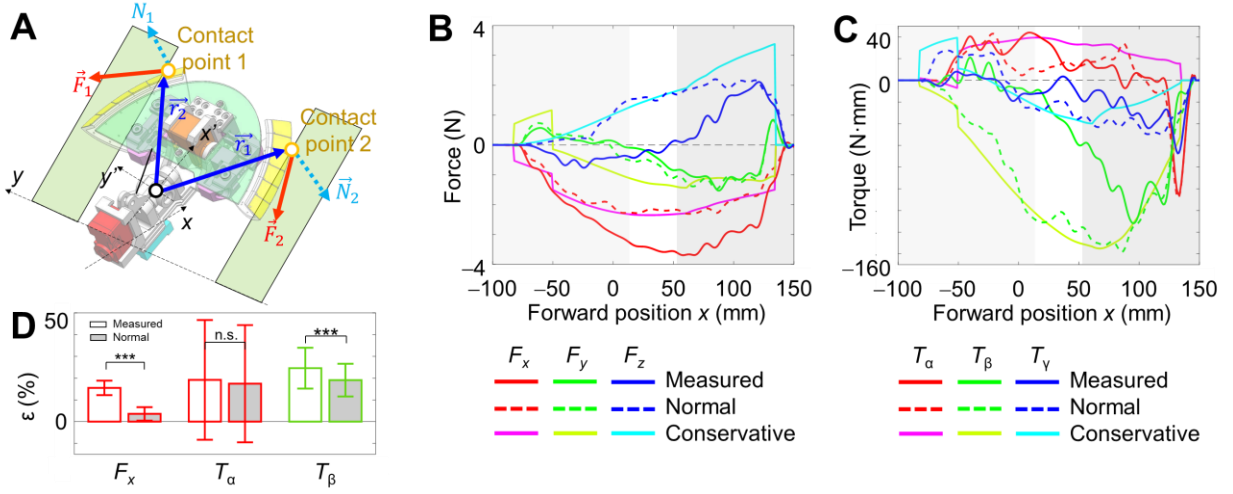


Fig. 4. Estimating the potential energy landscape gradients using measured contact forces and torques. (A) Schematic of force analyses. The robot directly obtained the measured contact forces F_i (red arrows) from custom 3-D force sensors and contact positions (orange points) from touch sensors. Normal forces N_i (cyan arrows) were defined as the component of contact forces along surface normal directions measured by the contact sensors. Force arms r_i (blue arrows) were the distance from the geometric center to the contact point. Measured or normal torques were the cross of force arms and measured ($T_i = r_i \times F_i$) or normal forces ($T_{i,N} = r_i \times N_i$), separately. (B and C) Measured, normal, and conservative contact (B) forces and (C) torques as functions of forward position x from a representative trial. Light and dark gray show where contacts with both beams are surface and edge contact cases, separately. (D) Relative error ϵ of using fore-aft force F_x , contact force roll torque T_α , and pitch torque T_β as the landscape gradients in surface contact cases. White and gray bars show measured and normal forces/torques, separately. See Section *Using normal forces and torques improves estimation of conservative ones in surface contact cases* in *Results* for definition of normal forces/torques. Bars and error bars are means ± 1 standard deviation of the average relative error of all average trials. *** $P < 0.001$, n.s.: not significant $P > 0.05$, Student's t-test.

Here, we further describe the evolution of the potential energy landscape as the robot traversed the beam obstacles (Fig. 2D) to help understand how these observed trends matched those expected from the

landscape. We defined the potential energy landscape similarly as in (9) (see Section *Potential energy landscape modeling* in *Materials and Methods*). Before encountering the beams, the system’s potential energy was simply the robot’s gravitational potential energy. Because the robot was bottom-heavy, the potential energy landscape formed a global basin in the roll-pitch (α - β) section, whose global minimum was at zero roll and zero pitch (i.e., the horizontal posture, $\alpha = \beta = 0^\circ$) (**Fig. 2D, i**). As the robot encountered and interacted with the beams, the average potential energy landscape in α - β section lifted, because more beam elastic energy was stored, and the system potential energy increased. The global basin evolved into a “pitch” basin, whose local minimum was at a negative pitch ($|\beta| = 0^\circ - 70^\circ$) and zero roll. At the same time, two “roll” basins emerged, whose local minima were at near-zero pitch and a positive or negative roll (around $\alpha = \pm 50^\circ$) (**Fig. 2D, ii, iii**). The pitch and roll basins separated by barriers (around $\alpha = \pm 35^\circ$) (**Fig. 2D, ii, iii**).

Comparing the trends of measured forces and torques with landscape evolution, we found that the direction of contact forces and torques along x , α , and β directions were always inverse to the corresponding landscape gradients. Specifically, (1) the system potential energy increased with x (**Fig. 2D, Video 1**, part 3), suggesting a positive gradient along the x direction. (2) The landscape gradients were near-zero when the robot’s state fell in the pitch basin and was near the local minimum (**Fig. 2D, ii, iii**, blue) at a small roll angle. (3) The landscape gradient along α direction was initially negative when the robot’s state was in the roll basin to the $+\alpha$ side of the barrier (**Fig. 2D, ii, iii**, red) at a large roll angle. (4) The landscape gradient along β direction was initially negative when the robot’s state was to the $-\beta$ side of the local pitch or roll minimum. As the robot moved forward, if $|\beta|$ was small, the landscape gradients along the β direction changed to positive as the landscape minimum shifted along $-\beta$ direction and passed the robot’s state.

The match between the trends of forces and torques and the landscape evolution suggested that the contact forces and torques were strongly related to the corresponding landscape gradients.

Measured contact forces and torques roughly matched landscape gradients

We further quantitatively compared the measured contact forces and torques with the conservative forces and torques (i.e., potential energy landscape gradients) from modeling, and found that they roughly matched each other (**Fig. 4B, C**, measured vs. conservative). The measured forces and torques matched conservative ones with a small relative error of $\varepsilon_x = 15\% \pm 3\%$ in the x direction, $\varepsilon_\alpha = 19\% \pm 28\%$ in the α direction, and $\varepsilon_\beta = 25\% \pm 9\%$ in the β direction (**Fig. 4D**, measured) (see Section *Comparison criteria and Statistics in Materials and Methods* for definition of relative error).

These results showed that, despite not being fully conservative, the measured contact forces and torques enabled potential energy landscape gradient estimation. We speculated that the mismatch between the sensed forces and torques and the landscape gradients was caused by friction, collisions, inertial effects, etc. See Section **S2** for theoretical proof that the contact forces and torques should be the landscape gradients without these factors.

Reconstructed potential energy landscape matched with ground truth

To test whether the measured contact forces and torques can infer the potential energy landscape, we performed Helmholtz decomposition (33) on them to reconstruct the landscape (see Section *Potential energy landscape reconstruction in Materials and Methods*). We found that the reconstructed landscape (**Fig. 5A**) and its gradients matched the ground truth from modeling (**Fig. 5B**) (also see **Video 1**, part 3) with a low relative error of $\varepsilon_{PE} = 14.0\%$ in potential and $\varepsilon_{Grad} = 21.6\%$ in gradients (see Section *Comparison criteria and Statistics in Materials and Methods* for the definition of relative error). By comparison, we also reconstructed the potential energy landscape using vision-based geometry sensing by assuming that beams are rigid (see Section **S3**), which had a much poorer reconstruction accuracy (relative error $\varepsilon_{PE} = 180\%$ in potential).

These results showed that the measured contact forces and torques enabled potential energy landscape reconstruction. We speculated that although the measured forces and torques were not fully conservative, the Helmholtz decomposition compensated the non-conservative parts and extracted a potential whose gradients best matched the measured forces and torques.

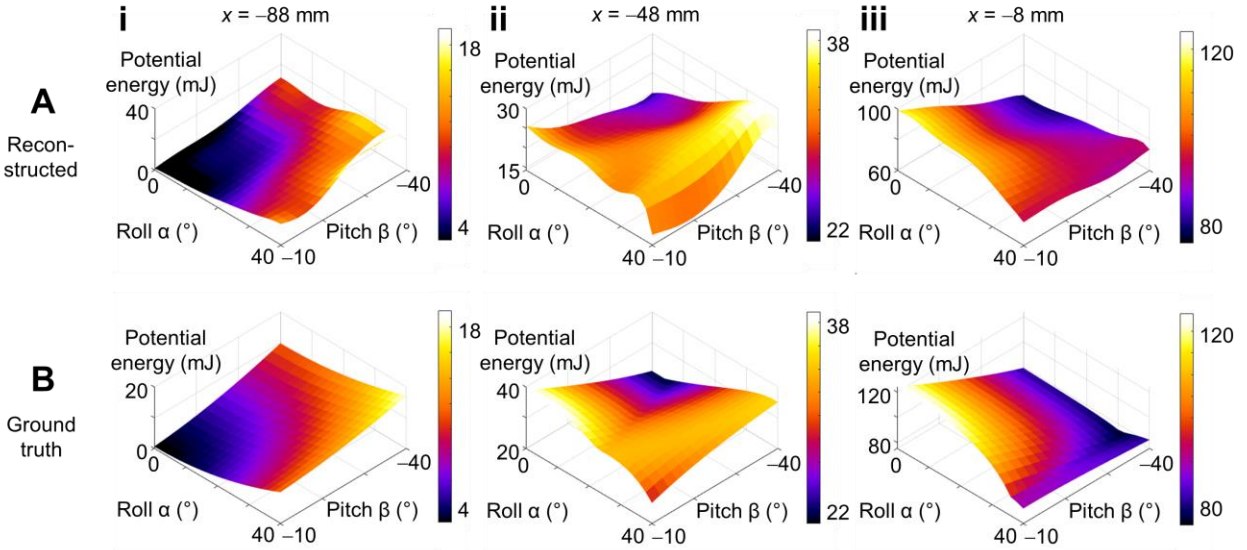


Fig. 5. Potential energy landscape reconstruction. (A) Reconstructed and (B) ground truth potential energy landscape evolved as the robot moved forward. The presented landscapes are from the trials without head oscillation ($f = 0$ Hz) as a demonstration. (i) $x = -88$ mm, (ii) $x = -48$ mm, (iii) $x = -8$ mm. The landscape figures in the same column share the same colormap range.

Using normal forces and torques improves estimation of conservative ones in surface contact cases

The contact between the robot and obstacles can be of two kinds: surface contact and edge contact, where the contact point is on a 2-D surface (Fig. 3B, yellow) or a 1-D edge (Fig. 3B, orange) of the robot, separately. The robot can easily identify the contact cases because it knows the triggered touch-sensitive cell. Both contact cases appear frequently (surface: $56\% \pm 16\%$, edge: $44\% \pm 16\%$ among all trials).

In the surface contact cases, because friction was one of the factors that caused a mismatch between sensed forces and torques and the conservative ones, we hypothesized that estimating the surface normal direction and using normal forces (i.e., the component of measured forces along the surface normal direction) and their torques to estimate conservative ones eliminated the effect from friction (component along the surface tangential direction) (see Section *Force analyses and accuracy optimization in Materials and Methods*). To verify this, we obtained the measured normal direction (Fig. 4A, same direction as cyan) as that of the triggered touch-sensory cell. We found that the measured normal direction matched well with

the ground truth, with a small estimation error of $8\% \pm 4\%$ in surface contact cases. We further calculated the normal forces and torques as the estimation of conservative ones. We found that the normal forces and torques better matched the conservative ones in the surface contact cases, reducing the estimation errors in the x direction to $\varepsilon_x = 4\% \pm 3\%$ from $16\% \pm 3\%$, and β direction to $\varepsilon_\beta = 19\% \pm 8\%$ from $25\% \pm 9\%$ ($P < 0.001$, Student's t-test). However, we found no significant improvement in the α directions ($P = 0.37$, Student's t-test) (**Fig. 4D**, normal vs. measured).

These results showed that using normal forces and torques improved landscape gradient estimation in surface contact cases. Besides, we also found that further improving the normal direction measurement accuracy promised better conservative forces and torques estimation (see Section **S6**). Further discussion on why using normal torques does not improve conservative torque estimation in α direction is in Section *Remaining issues in this study* in *Discussion*.

Active robotic head oscillation improves estimation of conservative forces and torques in edge contact cases

Although contact forces and torques are already good landscape gradient estimates, a robot or an animal benefits from a more precise landscape gradient estimation when traversing obstacles (See Section *Animal's head oscillation may allow active sensing of obstacle forces and torques* in *Discussion*). We attempt to learn from the animal behaviors to improve landscape gradient estimation. Curiously, the discoid cockroach often exhibits up/down head oscillations (more than on flat ground (18)) (**Fig. 6A, B**) while pushing against large obstacles before transitioning to easier modes to traverse (9, 14, 15, 18). We speculate that such motions may be “exploratory” (34) to help an animal or robot sense landscape gradients over a small neighborhood of its current state.

Specifically, we hypothesized that with a fast enough oscillation, the frictions in the back-and-forth motion cancel out each other when the oscillation frequency is filtered out. To verify this hypothesis, we controlled the robot to actively oscillate its head at a frequency of 2 Hz (which emulates the animal behavior after scaling, see Section **S7**) while traversing the beams, and compared the measured contact forces and

torques with the conservative ones. We found that as the head oscillation involved, the measured forces and torques (after flattening out the head oscillation frequency) usually converged to the conservative one in the edge contact cases (**Fig. 6C-E**). With head oscillation ($f = 2$ Hz), compared to without ($f = 0$ Hz), the measured forces and torques better matched the conservative ones in x direction, improving to $\varepsilon_x = 5\% \pm 4\%$ from $8\% \pm 3\%$ ($P = 0.0012$, Student's t-test), and β direction, improving to $\varepsilon_\beta = 17\% \pm 7\%$ from $31\% \pm 12\%$ ($P < 0.001$, Student's t-test), but no significant improvement was found in α direction ($P = 0.45$, Student's test) (**Fig. 6F**).

These results showed that active head oscillation improves landscape gradient estimation in edge contact cases and landscape reconstruction. Further discussion on why the active head oscillation does not improve conservative torque estimation in α direction is in Section *Remaining issues in this study* in *Discussion*.

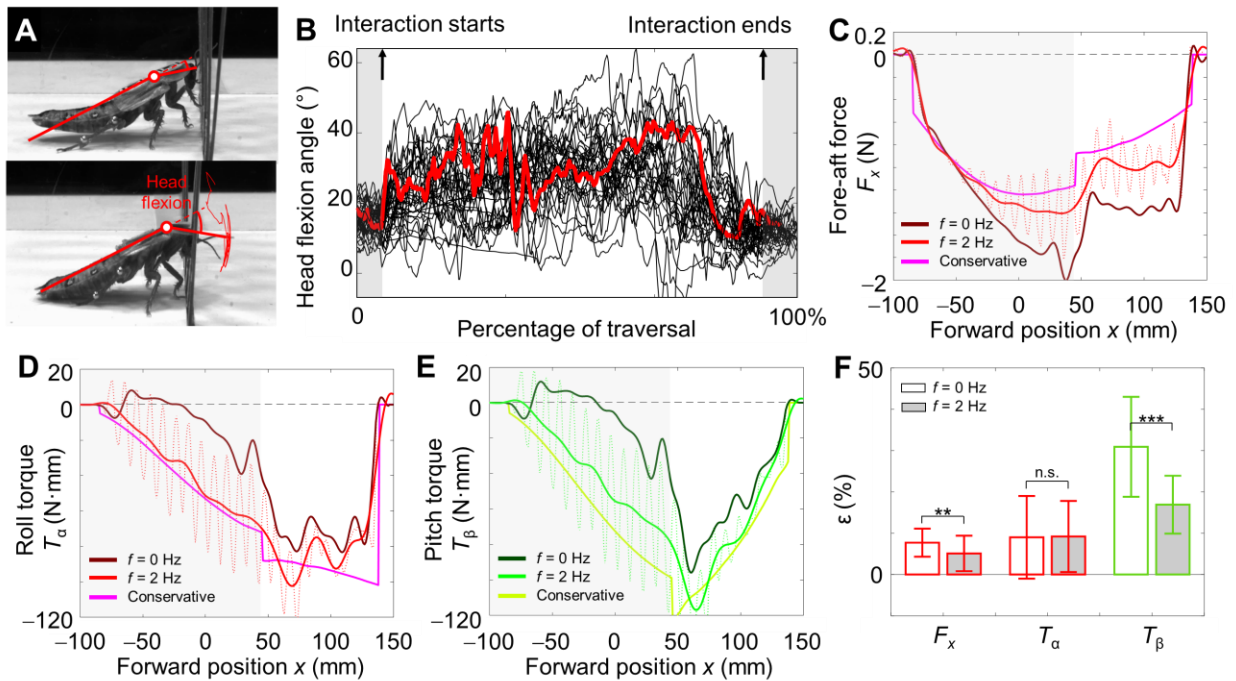


Fig. 6. Head oscillations modulated sensed contact forces and torques. (A) Snapshots of a cockroach oscillating its head while traversing cluttered large obstacles. Head flexion angle was defined as the relative pitch angle between the animal's head and thorax. Red curve shows representative head oscillation from a trial. (B) Head flexion angle as a function of traversal progress when a cockroach traverses large, cluttered

obstacles. Curves are individual trials. Thick, red curve is from the single trial in (A). White and gray backgrounds show the cockroach physically interacting with the obstacles or otherwise, separately. The cockroach oscillated its head in a larger amplitude when it physically interacted with the obstacles than otherwise. (C) Fore-aft force F_x , (D) roll torque T_α , and (E) pitch torque T_β as functions of forward position x from a representative trial. As the total roll torque (sum from both beams) was near zero, we show the forces and torques from contact with the right beam only for better comparison. In the case with head oscillation ($f = 2\text{Hz}$), thin, dashed curves are original, unfiltered data (see Section *Data filtering and averaging* in *Materials and Methods*), thick, solid curves are further processed by zero-phase digital filtering using a six-order Butterworth filter with a cut-off frequency of the corresponding head oscillation frequency for better comparison. Gray shows edge contact phase. (F) Relative error ε of using fore-aft force F_x , roll torque T_α , and pitch torque T_β as the landscape gradients in edge contact cases. White and gray bars show using measured force/torques without ($f = 0\text{Hz}$) and with ($f = 2\text{Hz}$) head oscillation, separately. Bars and error bars are means ± 1 standard deviation of the average relative error of all average trials. $***P < 0.001$, $**P < 0.01$, n.s.: not significant $P > 0.05$, Student's t-test. (A, B) are adapted from (18).

DISCUSSION

Major findings

In summary, we built a robot capable of sensing obstacle contact forces and torques. Using a model system of grass-like beam obstacle traversal, we found that such sensing enabled the potential energy landscape gradient estimation and landscape reconstruction despite the measured forces and torques not being fully conservative. We also found that using normal forces and torques and a robotic active head oscillation improved the accuracy of landscape gradient estimation. This initial step introduces the potential energy landscape modeling to unknown, cluttered large obstacles where the robot physically interacts with them, similar to how machine vision enables robots to apply artificial potential fields to avoid sparse obstacles.

Benefit from custom, distributed sensors

Although reconstructing potential energy landscapes only requires total contact forces and torques, where one six-axis force and torque sensor is sufficient, we used a combination of custom distributed force and contact sensors for multiple reasons. Firstly, these custom sensors are low-cost (~\$200 for all sensors and DAQ on our robot) and easy to repair (~10 min to repair one worn touch-sensitive cell) compared to a commercial sensor (~ \$8,000 for a transducer, repair cycle??), which suits fast prototyping. Secondly, this distributed sensor design is robust against sensor damage. For example, a single touch-sensitive cell damage does not affect force sensory, and only causes a minor error in contact point sensory information, which can also be easily mitigated from interpolation. Finally, the distributed force and contact sensors provide much richer information, such as contact force with either obstacle or local stress on the shell, that may be useful for future studies (e.g., as a robophysical model mimicking campaniform sensilla (35) on insect's exoskeleton to study how an insect leverage mechanoreception to sense and traverse obstacles. See Section *animal's head oscillation may allow active sensing and local potential energy landscape estimation averaging* in *Materials and Methods*). Moreover, compared with flexible sensory arrays (25–30), our hierarchical sensory strategy to have multiple distributed 3-D force sensors, each monitoring multiple contact sensors, can easily achieve a similar contact sensing resolution, and faster, more accurate, multi-axes force sensing.

Revealing potential energy landscape as a representation of the physical interaction with the obstacles

Although a previous review summarized that the potential energy landscape approach successfully modeled the locomotor-terrain physical interaction over many model obstacles and self-righting, and suggested that the robot (and animal) can identify distinct obstacles and transition to proper modes to traverse then one-by-one (10) (proved to be practical in (36)), many problems are unsolved to keep this approach from real applications, e.g., whether the potential energy landscape modeling can be generally applied to the physical interactions between any robots and any large obstacles; how to deal with the situation where the obstacles are too dense to separate (e.g., in **Fig. 1F**). Since the contact forces and torques are ubiquitous in physical interaction with the obstacles, and we found a relation to transform contact forces

and torques to a potential energy landscape (see Section **S9** for another example of successfully reconstructing potential energy landscape from obstacle contact force and torque measurement using another robot), we show that the potential energy landscape approach is applicable to all large obstacles (note that this claim does not indicate that the potential energy landscape dominated all obstacle interaction dynamics, see (10) for discussion on its limitation). Moreover, the relation also indicates that the potential energy landscape is a representation of the physical interaction with the obstacles, similar to a neural network serving as a general representation of complex mathematical formulas (37, 38). This inspires further studies to leverage other data-driven approaches (39) to identify the landscape in unknown environments, and provides simplified conceptual modeling of the physical interactions with obstacles as a starting point for control strategy development (see *Section How a free-running robot may use force sensing to facilitate transitions* in *Discussion* for an example).

Why and how head oscillation leads to better landscape gradient estimation

In each trial, the robot held its rotation and moved forward at a constant speed. We speculate that in that case, the system was dominated by normal forces and friction, whereas speed-dependent forces (e.g., damping forces) and inertial forces were small. In the edge contact cases, we speculated that the fast head oscillation made the contact friction cancel out temporally. When the robot's head was static (relative to the body), under a kinetic Coulomb friction assumption, the contact friction f was along the direction of relative velocity \vec{v}_0 between the body and the beam, and its amplitude depended on the normal contact force N and friction coefficient μ : $f = \mu |N| \frac{\vec{v}_0}{|\vec{v}_0|}$. When the robot head oscillated up and down, it added an oscillatory velocity $\pm \vec{v}_{add}$ to the original relative velocity between the body and beams, and the contact friction was along the direction of this new relative velocity as $\vec{v}_1^\pm = \vec{v}_0 \pm \vec{v}_{add}$ for upward and downward head motion separately. When the head oscillation frequency is large enough, \vec{v}_{add} dominated the relative velocity, which made the latter roughly the same amplitude and inverse direction in the back- and forth-

motion, $\overline{v_1^\pm} \approx \pm \overline{v_{add}}$, and so did the friction, which canceled out each other when averaged temporally. Thus, the sensed contact forces and torques were closer to the conservative forces and torques.

Note that, in the surface contact cases, a head oscillation may not significantly improve the normal direction estimation, because the actuated motion may be perpendicular to the friction direction, so the friction won't cancel out. On the other hand, we also observed that the animal's whole body had obvious body oscillation in the fore-aft and lateral direction (9, 14, 18). We speculate that in a similar mechanism, these oscillations broke the friction and modulated the contact forces and torques to be closer to the landscape gradient. Further studies can test this by applying body oscillations in fore-aft and lateral directions and observing how they modulate the force and torque sensory.

Animal's head oscillation may allow active sensing and *local* potential energy landscape estimation

For obstacle traversal in real robotic applications and animal cases, the robot and the animal should estimate the local shape of the potential energy landscape (i.e., locally reconstruct the potential energy landscape) by estimating the conservative forces and torques and plan a prospective least-resistant path (this process could be simplified and encoded in the animal's neural network). However, unlike long-range vision or finite-range antenna sensing (40), force and torque sensing require direct contact. To estimate a potential energy landscape, a robot or an animal must move around the neighborhood of its current state and collect sensory data. However, unlike in our experiment, where the robot freely swept a large state space and used a global algorithm (e.g., Helmholtz decomposition) to compensate for the non-conservative forces and torques, with only a rough and quick exploration in local space, the robot or the animal cannot easily extract the conservative forces and torques due to limited samples. They have leveraged other information (e.g., geometry) and active motion (i.e., active sensing behavior) to obtain the conservative forces and torques in local space.

Previous biological studies in contact-based active sensing behavior (34, 41, 42) show that animals' force sensing inherently involves sensor motion, i.e., animals often move their sensors to enhance sensation. For example, when encountering an obstacle, an insect uses its antennas to repeatedly touch the obstacle

(e.g., cockroach (43, 44)) or does an antenna search and sample behavior aided by body and head rotating (e.g., stick insect (45, 46)), which locates the obstacle and induces turning to avoid collision (43, 46, 47); a rat actively whisks (i.e., moving the whiskers back and forth) against objects when exploring the environment (48–51). From comparative robotic studies (52–54), this probably enables the animal to extract object contours (55, 56). We speculate that similarly, the discoid cockroach’s head oscillation in beam obstacle traversal (9, 18) suggested a novel form of active sensing, which is useful for freely moving robots traversing cluttered large obstacles.

Although our study shows that a similar robotic head oscillation modulated force and torque sensory signals to better capture the physical interaction with the obstacles (in the form of potential energy landscape gradient), whether and how the animal leverages a similar mechanism during obstacle traversal remains not understood. To test this speculation, future studies should measure the animal’s muscle activity and neural signals to first verify whether the head oscillation behavior is active or passively resulting from obstacle interaction. If it is an active behavior, studies can collect more biological observations and use robophysical models to examine the function of this behavior.

How a free-running robot may use force sensing to facilitate transitions

We speculate that our strategy to sense contact forces and torques to estimate landscape gradients and reconstruct the landscape will work in free-running robots. Because traversing cluttered large obstacles is highly strenuous, the robot needs to continually push against and intermittently collide with them (10), making it difficult to build up high momentum, i.e., it operates in a low-speed, small-acceleration regime, where the speed-dependent damping forces and inertial forces are likely small. Also, the robot often makes intermittent body contact with and pushes against large obstacles, likely resulting in large normal forces, whereas the associated frictional forces are usually smaller. Based on these, it is plausible that the conservative forces dominate the noisy contact forces even for a freely running robot, and our approach still applies.

Towards this, we still need to solve major additional questions. Firstly, how to filter the noisy contact forces with the obstacle to infer the landscape gradients. When a self-propelled, free-moving legged robot (36) negotiates with obstacles, the force sensory data can be substantially noisy because of friction and damping, oscillation from cyclic leg propulsion, and impulse from frequent collision with the beams. Studies can look for better mechanical design or signal processing methods to obtain the landscape gradients and reconstruct the landscape from the noisy sensory data.

Secondly, how to use sensing to reconstruct the *local* landscape near the robot's trajectory to enable a single, "zero-shot" traversal. Future studies can adopt bio-inspired approaches. For example, cockroaches (9, 14, 18, 57) and ground beetles (58) often like to wedge in between obstacles like shrubs or rock cracks to go in to seek shelter. It is plausible that these animals use proprioceptive and tactile sensing (59, 60) to detect or infer the obstacle resistance or resistive forces as they do so (18). If this were the case, using such exploratory motions may allow these animals to sample contact forces and torques around their neighboring states and decide a direction with the least resistance to maneuver through/into the gaps/cracks. In other words, such animals' preference to go towards weaker spots (if they have such preference) coupled with exploratory motions for force and torque sensing may lead them to follow small potential energy gradients to ascend towards saddles and make least-effort transitions (61, 62). We speculate that the robot can use a similar bio-inspired approach to actively sample around neighboring states to reconstruct a local landscape, estimate and follow the lowest gradient direction to gradually find saddles, and make least-effort transitions to traverse obstacles. Future studies can also combine vision (or geometry detection) with force and torque sensing to enlarge local landscape detection region, and adapt other numerical algorithms for finding saddles and maximum-likelihood transition paths between local stability basins in physical chemistry (62–67).

Ultimately, we hope to build on this initial sensing and landscape reconstruction work to enable self-propelled, free-moving robots, during a single, "zero-shot" (68) traverse with substantial sensing noise, to use a range of exploratory motions to sample forces and torques around its current state, estimate and

follow the lowest gradient direction and follow it to gradually find saddles, and control its self-propulsion to cross saddles to make least-effort transitions to traverse cluttered large obstacles.

Full modeling of stochastic dynamics in large obstacle traversal

Building on the potential energy landscape modeling, future studies should model the robot (and animal) locomotion during cluttered large obstacle traversal as a potential energy landscape-dominated, stochastically perturbed dynamics with diffusion (i.e., Langevin dynamics (69–71)), where friction, damping, kinetic energy fluctuation, and inertia effects will also be considered (10). The Langevin equations will greatly improve the prediction of the system dynamics, especially in the neighborhood of the saddle point, because around saddle points, the potential gradients are near zero, and the friction, damping, and oscillation will dominate the robot dynamics. Reliably producing Langevin dynamics models will improve our understanding of biological motion and create new possibilities for robot control in challenging environments.

Remaining issues in this study

Currently, the distributed touch-sensory cells require the obstacle surface to be conductive (and better be grounded), which limits its access to nature. They are also worn out due to consistently rubbing against the obstacles (in ~100 trials of experiments). We should seek other touch detection mechanisms (e.g., dome switch (72)) for out-of-lab applications.

The potential energy landscape reconstruction did not show steep gradients near the barrier like the ground truth (**Fig 5, iii**, around roll $\alpha = 35^\circ$). We speculate that this was because the state space of the steep gradients was small, and insufficient samples were taken in the neighborhood. A possible solution is to obtain more samples in the region with steep gradients.

Neither using normal roll torque nor involving head oscillation improved roll torque estimation. We speculated that this was because the pitch basin was flat along the roll direction, where the conservative roll torque was near zero, and the friction-resulted torque dominated the measured roll torque. We speculate

that this can be better explained using Langevin dynamics (see Section *Full modeling of stochastical dynamics in large obstacle traversal* in *Discussion*).

Envision torque sensing guiding self-righting

As the potential energy landscape modeling also reveals physics principles of self-righting of animals and robots (73, 74), we foresee that torque sensing can guide better self-righting. Because the potential energy landscape of self-righting varies dramatically with the ground geometry (73), we envision that the capability of reconstructing the potential energy landscape on an unknown ground will benefit the animal or the robot by identifying the least-effort rotating direction to apply direct perturbation to self-right. Because self-righting only involves rotational dimensions, sensing ground reactive torque is sufficient for landscape reconstruction. However, self-righting is highly dynamic and unavoidably involves fierce perturbation from wing opening and leg flailing. Therefore, the inertial effect and impulses can heavily bias the sensed ground reactive torque.

MATERIALS AND METHODS

Potential energy landscape modeling

The system's potential energy PE was the sum of the gravitational potential energy of the robot PE_G and the elastic potential energy from the beams PE_E :

$$PE_G = mg(\Delta z - h),$$

$$PE_E = \frac{1}{2} k_1 \theta_1^2 + \tau_1 \theta_1 + \frac{1}{2} k_2 \theta_2^2 + \tau_2 \theta_2,$$

$$PE = PE_G + PE_E = mg(\Delta z - h) + \frac{1}{2} k_1 \theta_1^2 + \tau_1 \theta_1 + \frac{1}{2} k_2 \theta_2^2 + \tau_2 \theta_2,$$

where m was the mass of the robot, g was the gravitational acceleration, Δz was the vertical distance between the geometric center and center of mass, $\theta_{1,2}$, $k_{1,2}$, and $\tau_{1,2}$ are the deflection angles, the torsional stiffness, and the preload of the left and right beams, separately. See Section **S1** for more details.

Robot experiment protocol

Before each trial, the robot was positioned at a distance of 200 mm ($x = -200$ mm) from the beams, at a height of $z = 138$ mm, roughly in the midline ($y = -6$ mm) and pointing forward ($\gamma = 0^\circ$). The robot feed-forwardly rotated to the requested roll and pitch angle. The beams were set vertically and moved to have a gap of 130 mm wide symmetric to the midline. The robot's head was aligned with the body (head angle = 0°). All the force sensors were zeroed. Then, the robot's head started oscillating between 0° and 20° at a frequency of f (for $f = 0$ Hz) until the end of the fore-aft translation, and the LabVIEW program started data recording. After a random period (to randomize the head oscillation phase), the robot was actuated to move forward at a constant speed of $20 \text{ mm}\cdot\text{s}^{-1}$ by a distance of 500 mm, which guaranteed the robot passed the beam obstacle area fully, and the beams were bounced back to vertical. Finally, we stopped the head oscillation and data recording and moved the robot back to its initial position for the next trial. Two cameras (Logitech C920 HD PRO, Logitech, Switzerland) synchronized by Open Broadcaster Software (OBS) recorded the experiment from the side and the isometric views at a frame rate of 30 Hz and a resolution of 960×720 pixels.

We varied the head oscillation frequency f at 0 and 2 Hz. For head oscillation frequency f , we varied the desired roll angle α from 0° to 40° with an increment of 5° and the desired pitch angle β from -10° to -40° with a decrement of 5° (note that negative pitch angle meant heads-up). At each combination of head oscillation frequency f , desired roll angle α , and pitch angle β , we performed five trials, which resulted in a total of $n = 630$ trials.

Note that due to the robot frames and links were not excessively stiff, the robot's roll and pitch angles slightly changed (maximum roll angle change $< 10^\circ$, maximum pitch angle change $< 5^\circ$) in each trial. We measured the roll and pitch angles from IMU to account for this effect.

Force analyses and accuracy optimization

The measured contact forces (**Fig. 4A**, red) are directly measured from the 3-D force sensors. The contact position (**Fig. 4A**, orange points) was estimated as the center of the cell at the contact. In detail, every cell on the robot shield-shaped surface (i.e., not on the edge) is a quadrilateral (**Fig. 3D**), which is

from two fractions of an ellipsoid. The center is calculated as the average of the four corners and projected to the ellipsoidal surface. The measured normal direction was defined as that at the center of the cell at contact, which was obtained based on the full acknowledgment of the shell shape. The normal force (**Fig. 4A**, cyan) was the component of the measured force along the normal direction. The force arm (**Fig. 4A**, blue) was the distance from the robot's geometric center to the contact position. The measured or normal torque was the cross of the force arm and the measured or normal force, separately. The measured or normal torques along the roll, pitch, and yaw direction were the projections of the torque T along the roll (x' -, as yaw is zero), pitch (y -, as yaw is zero), and yaw (z -) axes, separately. The total measured and normal forces and torques were the sum of those from the two beams. We don't define normal direction, forces, and torques in the edge contact cases. Note that in this section, we made no assumption about the obstacle geometry nor requested any obstacle properties or motion information, which indicates that these analyses are adaptable to various obstacles.

To optimize the estimation of contact position and normal direction, we minimized the maximum estimation error over the entire surface. The maximum estimation error of contact position and normal direction were assumed to be at one of the four corners. We calculated the maximum position error (defined as the maximum distance from any point on the cell to the cell center) and maximum normal direction error (defined as the maximum angle between the normal directions from any point on the cell and cell center) on each cell as sensory resolution, and revised the pattern of the sensory cells to minimize the largest resolutions of the two aspects over the entire surface.

Data filtering and averaging

All the data (robot positions, orientations, head oscillation angles, forces, torques, etc.) were processed by zero-phase digital filtering (i.e., "filtfilt" function in MATLAB) using a six-order Butterworth filter with a cut-off frequency of 6 Hz ($f = 2\text{Hz}$), 1.5 Hz ($f = 0\text{ Hz or } 0.5\text{ Hz}$), or 3 Hz ($f = 1\text{ Hz}$) (See Section **S7** for head oscillation frequency selection). As the measured data are consistent using the same treatment (see Section **S8** for limited exceptions), to obtain the average data, we varied the x from -100 mm to 200

mm with an increment of 1 mm, and we linearly interpolated the measured data over x and then averaged them over the five repeated trials.

Potential energy landscape reconstruction

We used the measured contact forces and torques to estimate the vector field of landscape gradients in the x - α - β space, combining all averaged trials. Due to the slight change in the robot’s roll and pitch in each trial (see Section *Robot experiment protocol* in *Materials and Methods*), the vector field base was heterogeneous (i.e., not strictly gridded). We applied a meshless Helmholtz-Hodge decomposition (HHD) (75) on this vector field to reconstruct the potential energy landscape. Only the landscape for x from -100 mm to 100 mm was reconstructed because our landscape model did not capture the beam bouncing back after that range. To roughly unify the input data along the three axes, we multiplied a ratio of 0.01 to the input bases \mathbf{X} along x -axis and multiplied the reciprocals of this ratio to the input vectors $f(\mathbf{X})$ along x -axis so that the multiplication of the unit of the base and vectors—the potential energy—was unchanged. We chose a commonly used Gaussian kernel function $\phi_i(\mathbf{X}) = \exp(-\sigma r_i(\mathbf{X})^2)$, where $r_i(\mathbf{X})$ was the Euclidean distance between the base \mathbf{X} and the i -th center in the unified x - α - β space, because this kernel function fit the expected continuous, 1-order smooth, non-periodic landscape. We generated the $k = 2000$ centers by performing k -means clustering on the input base \mathbf{X} . This kernel number k allows robust estimation results (from a preliminary test, no significant performance reduction with even 60% data loss). We rejected any centers close to any input base \mathbf{x} ($< 10^{-4}$ unit) to avoid singularity in the calculation. See Section **S5** for algorithm details.

Note that the meshless Helmholtz decomposition also involves errors in landscape reconstruction. Even when performed on the conservative forces and torques, the landscape estimation still has a smaller relative error of $\varepsilon_{PE} = 2.1\%$ in energy and $\varepsilon_{Grad} = 12.5\%$ in gradients.

Comparison criteria and statistics

When comparing the measured data or reconstructed landscape with the model, we were only interested in the period when the robot interacted with the beam obstacles. Here, we defined two fore-aft positions: the attach position x_a , where the robot first contacted all the beams, and the detach position x_d , where the robot first detached from one of the beams and the beam bounced back. For each trial, the attach position x_a was identified as x at the first time frame where both the beam angles θ are bigger than a threshold of 3° ; the detach position x_d was identified as x at the first time frame where either of the beam angle θ reached maximum.

To compare fore-aft force F_x , roll torque T_α , and pitch torque T_β to the model, we only chose the data from the attach position x_a to the detach position x_d . We averaged the absolute difference between the measured data and model over x and divided it by the maximum range of the model data to obtain a relative error:

$$\varepsilon = \frac{\overline{|y(x)-r(x)|}}{r(x)_{max}-r(x)_{min}} \times 100\%,$$

where ε was the relative error, $y(x)$ was the measured data, and $r(x)$ was the model as reference. We used this criterion instead of a traditional relative error definition because the model data had near-zero sections. To compare the measured potential energy landscape in x - α - β space to the model, we flattened the landscapes into 1-D (i.e., function “reshape” in MATLAB) and defined the relative error the same as above. To compare the measured landscape gradients in x - α - β space to the model, we first unify the data along the three axes by dividing the gradients along the x direction by 0.01 (see Section **Potential energy landscape reconstruction** in **Materials and Methods**), then flattened the gradients into a row of vectors (i.e., function “reshape” in MATLAB), and defined the relative error using the maximum norm of model data as the denominator:

$$\varepsilon = \frac{\overline{|y(x)-r(x)|}}{|r(x)|_{max}} \times 100\%.$$

All average data are reported as mean \pm 1 standard deviation. We used Student’s t-tests to test whether the normal direction estimation or increasing head oscillation frequencies enabled a better estimation of the landscape gradients or landscape reconstruction performance. All the analyses except for

statistical tests were performed using MATLAB R2021b (MathWorks, MA). All the statistical tests were Student's t-tests performed using JMP PRO 17 (SAS Institute Inc., NC).

Acknowledgments

We thank Ratan Othayoth for sharing CAD files for previous robot system design and discussion on experiment conduction; Xiao Yu for help in assembling the experimental setup and preliminary testing; Qihan Xuan for discussion on experiment design and conduction; Shai Revzen for discussion on experiment design and saddle finding algorithms; Ioannis Kevrekidis, and Anastasia Georgiou for discussions on saddle finding algorithms; Noah Cowan, Jean-Michel Mongeau, Jeremy Brown, and Mitra Hartmann for discussion on active sensing.

Funding

This work was supported by a Beckman Young Investigator Award from Arnold and Mabel Beckman Foundation for CL, a Career Award at the Scientific Interface from Burroughs Wellcome Fund for CL, a Bridge Grant from Johns Hopkins University Whiting School of Engineering for CL, and a Research Experience for Undergraduates in Computational Sensing and Medical Robotics (CSMR REU) from National Science Foundation for LX and CL.

Author contributions

Y.W. and C.L. designed research; Y.W. performed research; L.X. contributed new methods; Y.W. analyzed data; and Y.W. and C.L. wrote the paper.

Competing interests

Authors declare that they have no competing interests.

Data and materials availability

The robot and experimental system’s CAD models, control codes, and experiment data are available from GitHub after the publication of the article: https://github.com/TerradynamicsLab/landscape_reconstruct.

Supplementary Material

S1. Potential energy landscape modeling

To theoretically generate the potential energy landscape as ground truth, we approximated the robot’s shell as its uncropped counterpart. The robot’s center of mass $m = 0.53$ kg was assumed to be at $h = 8$ mm below the geometric center, similar to that of the previous study (9). Each beam was modeled as a massless rigid rectangular plate on a preloaded Hookean torsional joint without damping. For a given robot position and orientation, each beam’s deflection angle was calculated as the largest possible forward deflection angle that let the beam contact with the robot, or zero if no such angle existed. Therefore, the beam deflection angles and the elastic potential energy fully depend on the robot’s position and orientation. As the system potential energy is the sum of the gravitational potential energy of the robot, the elastic potential energy from the beam, the potential energy landscape depends on the robot’s position (x, y, z) and orientation (roll α , pitch β , yaw γ). To calculate the landscape gradients, we took a central differentiation of the potential energy landscape along $\{x, y, z, \alpha, \beta, \gamma\}$ with a 10^{-4} unit perturbation.

S2. Proof that obstacle contact forces and torques are negative potential energy landscape gradients

In this proof, we assume that the robot and obstacles move quasi-statically, and there is no friction or damping. The system has no kinetic energy, and the input work is all transformed into potential energy:

$$W = \Delta PE,$$

where W is the input work, and ΔPE is the change of the system's potential energy. Examples of the input work are the propulsion from legs or air thrusters. As the robot moves quasi-statically, the equilibrium equations hold:

$$F_{G, q_i} + F_{OB, q_i} + F_{W, q_i} = 0, q_i \in \{x, y, z, \alpha, \beta, \gamma\},$$

where F_{G, q_i} , F_{OB, q_i} , and F_{W, q_i} are the gravitational, obstacle contact, and external input forces or torques along x, y, z, α, β , or γ axes, separately. The external input forces and torques are the partial derivatives of the input work:

$$F_{W, q_i} = \frac{\partial W}{\partial q_i}.$$

From classical mechanics, the system's potential energy is the integral of conservative external forces and torques along relevant degrees of freedom, $PE(X) = - \int_{X(0)}^X \vec{q}(\vec{X}) \cdot d\vec{X} = - \int_{X(0)}^X \sum_i q_i(X) dX_i$, where PE is potential energy (which includes gravitational and elastic potential energy in beam traversal), $\vec{X} = (x, y, z, \text{roll}, \text{pitch}, \text{yaw})$ is the state vector, and \vec{q} is the generalized force. We get that the negative gradients of the potential energy are the sum of gravitational and obstacle contact forces or torques:

$$\frac{\partial PE}{\partial q_i} = -(F_{G, q_i} + F_{OB, q_i}).$$

We assume that the robot's position and orientation are sensible. Gravitational force and torque can be obtained. We can calculate the obstacle contact forces and torques as follows:

$$F_{OB, q_i} = - \left(\frac{\partial PE}{\partial q_i} + F_{G, q_i} \right), q_i \in \{x, y, z, \alpha, \beta, \gamma\},$$

which supports our argument that the obstacle contact forces and torques are the negative potential energy landscape gradients, biased by the gravitational force and torque.

Note that although the contact forces and torques are the negative gradients of the potential energy from the obstacle ($F_{OB, q_i} = - \frac{\partial PE_{OB}}{\partial q_i}$) for this beam traversal problem, this does not apply to other obstacle traversal problems, e.g., in the bump (16), gap (17), and pillar (15) traversal, where the obstacle does not possess potential energy.

S3. Potential energy landscape based on geometry

To examine whether force and torque sensing enabled a potential energy landscape reconstruction better than geometry-based sensing, we generated a potential energy landscape assuming the beams were rigidly fixed, which should be the landscape reconstructed from perfect geometry-based sensing. Here, if we still assumed that the robot only moved in x - α - β space, we cannot appropriately define a finite potential energy when the robot had to penetrate a beam. Instead, we assumed that the robot adjusted its vertical position z to avoid the beams. The robot's gravitational potential energy at the minimum possible z was defined as the system's potential energy.

S4. Robot design and manufacturing

System design. The experiment system (**Fig. 3A**) consisted of the robotic physical model (**Fig. 3B**), a fore-aft sliding structure (outside **Fig. 3A**) that actuated the robot to move along the fore-aft (x -axis) and vertical (z -axis) directions, and two flexible beams (**Fig. 3A**, green), whose bases moved along the lateral (y -axis) direction. The robot had a body and a head (**Fig. 3B**). The body consisted of a frame, a gyroscope mechanism, and links to control rotation. The head consisted of a frame, two pieces of front shell, two custom 3-axis force sensors (**Fig. 3B**, magenta), and a self-designed data acquisition board (DAQ, **Fig. 3B**, green).

The shell was cropped from a shield-shaped counterpart (**Fig. 3B**, semi-translucent green), whose geometric centers were at the robot's origin at zero head angle. The shell was separated from the middle, which ensured that each part of the front shell only contacted one of the beams. Only the beam-contactable area and a small outer margin were reserved. To best compare with the previous study (9), the axe lengths of the shell's counterpart were kept the same as the previous design.

The two beams were made and characterized using the same method as in (9). Each beam was a rigid acrylic plate (30 mm width \times 200 mm height) attached to the base via a 3-D printed torsional spring joint. The beams only allowed forward deflection. The stiffest beams in (9) were used to maximize the beam contact forces and the force sensors' signal-to-noise ratio.

Actuation. The robot was fully actuated to rotate along roll and pitch direction (Euler angle follows the Tait-Bryan convention) and oscillate its head. To easily control the robot to rotate to the desired roll and pitch angles, we designed a gyroscope mechanism at the robot's origin of the body frame and added two servo motors (DYNAMIXEL XC330-M288-T, ROBOTIS Co., South Korea) to separately control the roll (**Fig. 3A, B**, red) and pitch angles (**Fig. 3A, B**, blue). To enable head oscillation, we connected the body frame and the head frame via a servo motor (DYNAMIXEL XC330-M288-T, **Fig. 3A, B**, pink) and used its encoder to monitor the head oscillation angle with a precision of 0.1° . The fore-aft sliding structure's motion and beam bases' motions were each powered by a servo motor (DYNAMIXEL XM430-W210-T, ROBOTIS Co., South Korea) via a gear-rack mechanism, and the motors' encoders directly obtained the displacements with a precision of 0.01 mm. All the servo motors were commended and reported their rotation angles to a microcontroller (OpenCM 9.04, ROBOTIS Co., South Korea) at a frequency of 50 Hz.

Data collection. To obtain contact forces with the obstacles, the load cells with a labeled range of ± 20 N and a precision of ± 0.004 N (BF-02088B, HK Bingf Sci. & Technol. Corp., China) in custom 3-D force sensor were read by the load cell amplifier chips (HX711, Avia Semiconductor, China) on the DAQ board. To obtain contact position, the touch sensory cells were connected to capacitive touch sensor chips (MPR121, Freescale Semiconductor, TX) on the DAQ board via a single wire and a pull-up resistor. When a cell contacted the grounded beam surface, the capacitive touch sensor detected the touch as a voltage drop. To monitor robot's rotation, we put an inertial measurement unit (IMU, **Fig. 3B**, cyan, BNO055, Adafruit Industries, NY) on the robot body and connected it with the DAQ board. A preliminary test showed that the IMU provided a good rotation measurement with errors $< 8^\circ$ and $< 2^\circ$ roll and pitch directions, separately. All the contact forces and positions and robot rotation sensory data were gathered by a microcontroller (Teensy 4.0, PJRC, OR) on the DAQ board at a frequency of 50 Hz.

The robot was attached to the hanging frame via an extra custom 3-D force sensor to monitor the hanging and propelling force. The force sensor consists of three load cells (5kg load cell, ShangHJ, China) serially connected and orthogonal to each other. With the load cell amplifier chip (HX711), each load cell could provide a separate force measurement along the lab x -, y -, or z -axis, with a labeled range of ± 50 N

and a precision of ± 0.02 N. To measure the beam deflection angles, we attached a potentiometer (100 K Ohm Potentiometer, HiLetgo, China) to each beam's rotational joint via a parallel four-bar linkage. The two end terminals were powered at 5 Volt, and the voltage at the wiper was measured to calculate the rotation angle with a precision of 0.3° . The force sensory data from the top sensor and the beam angles were collected by a microcontroller (Arduino Mega, Arduino, Italy) at a frequency of 50 Hz.

Calibration. See Section *Contact force and torque sensor design and calibration* in *Results* for load cell calibration. Because the bias shifted every time the DAQ restarted, we zeroed all force sensors before each trial of experiments. We characterized torsional stiffness and preload of the beams by measuring the restoring torque about the joint as a function of joint deflection angle using a 3-axis force sensor (Optoforce OMD-20-FG, OnRobot, Denmark), similar to (9). Torsional stiffness and preload of either beam were calculated from the slope and the intercept of the linear fit of the torque as a function of the deflection angle, which was $285 \text{ N}\cdot\text{mm}\cdot\text{rad}^{-1}$ and $91 \text{ N}\cdot\text{mm}$ for the left beam and $324 \text{ N}\cdot\text{mm}\cdot\text{rad}^{-1}$ and $77 \text{ N}\cdot\text{mm}$ for the right beam.

Visualization. We used a LabVIEW program to bidirectionally communicate with the microcontrollers and record experimental data at a frequency of 50 Hz. The LabVIEW graphical user interface (GUI, see **Video 1**, part 1, 2) allowed us to check all the sensory information (i.e., the robot's position, orientation, head oscillation angle, force amplitudes, and contact positions on each piece of front shell, propelling force, and the beams' positions and deflection angles) and manually control the system in real time, and conduct automatic pre-programmed experiments.

S5. Meshless Helmholtz-Hodge decomposition

The idea of Helmholtz-Hodge decomposition (33) was to consider the vector field as a sum of a gradient vector field (i.e., curl-free) and a solenoidal vector field (i.e., divergence-free):

$$f(\mathbf{X}) = g(\mathbf{X}) + r(\mathbf{X}) = -\nabla\Phi(\mathbf{X}) + \nabla\times A(\mathbf{X}),$$

where \mathbf{x} was the independent variable vector, or the base of vectors (e.g., $\mathbf{X} = [x, \alpha, \beta]$ in our case), $\mathbf{g}(\mathbf{X})$ was the gradient vector of a scalar potential $\Phi(\mathbf{X})$, $\mathbf{r}(\mathbf{X})$ was the solenoidal vector, which was a curl of the vector potential $A(\mathbf{X})$. We used the scalar potential Φ as the estimated potential energy landscape.

In meshless Helmholtz-Hodge decomposition (75), the scalar potential $\Phi(\mathbf{X})$ and the vector potential $A(\mathbf{X})$ were approximated as a linear combination of kernel function ϕ of a group of scattered points (centers):

$$\Phi = \sum_{i=1}^k a_i \phi_i,$$

$$A = \sum_{i=1}^k [b_{i,1} \phi_i, b_{i,2} \phi_i, b_{i,3} \phi_i]^T = \sum_{i=1}^k (\phi_i I) b_i,$$

where k was the number of centers, ϕ_i was the kernel function at the i -th center, a_i and $b_i = [b_{i,1}, b_{i,2}, b_{i,3}]^T$ were its coefficients of the linear combination, and I was a 3×3 identity matrix. At a given base \mathbf{X} , the gradients $f_g(\mathbf{X})$ and solenoidal $f_s(\mathbf{X})$ vector field were represented by the gradients of kernel function:

$$f_g(\mathbf{x}) = \sum_{i=1}^k a_i \nabla \phi_i = (\nabla \Phi)^T a,$$

$$\text{where } \nabla \Phi := [\nabla \phi_1, \dots, \nabla \phi_k]^T, a := [a_1, \dots, a_k]^T,$$

$$f_s(\mathbf{X}) = \sum_{i=1}^k \nabla \times \phi_i I b_i = (\nabla \times \Phi I)^T b,$$

$$\text{where } \nabla \times \Phi I := \begin{bmatrix} \nabla \times \phi_1 I \\ \dots \\ \nabla \times \phi_k I \end{bmatrix}_{3k \times 3}, b := [b_{1,1}, b_{1,2}, b_{1,3}, \dots, \dots, b_{k,1}, b_{k,2}, b_{k,3}]^T.$$

We speculate that the meshless landscape reconstruction algorithm we applied suits applications of a legged mobile robot that moves on cluttered terrain. In these cases, the robot's motion is also affected by the interaction with the obstacles, and the robot usually cannot freely and systematically vary its translation or rotation. The force sensory data can be heterogeneously scattered in the state space and sometimes missing in time series, which hinders applying reconstruction algorithms that need evenly gridded data (76–80). In contrast, the nature of the meshless algorithm handles the fragmented sensory data and allows for reconstructing the landscape locally in the state space, which is sufficient for most state-feedback controllers (see Section *How a free-running robot may use force sensing to facilitate transitions* in *Discussion* for details).

S6. More accurate normal direction measurement allows better landscape gradient estimation

Although we already elaborated that using normal forces and torques improves the estimation of conservative ones compared with directly using the measured ones, here we hypothesize that more accurate normal direction measurement further improves the estimation. To test this, we obtained the normal direction from modeling (estimation error $\varepsilon_{ND} = 0$ as the upper limit of normal direction measurement accuracy), calculated the force component along this direction and resulting torques (mentioned as semi-measured normal forces and torques) as the estimation of conservative ones. We found that in surface contact cases, compared to measured normal forces and torques, the semi-measured ones further improved matching in β direction to $\varepsilon_{\beta} = 5\% \pm 3\%$ from $19\% \pm 8\%$ ($P < 0.001$, Student's t-test) but no significant improvement in the x direction ($P = 0.07$, Student's t-test) (**Fig. S1**).

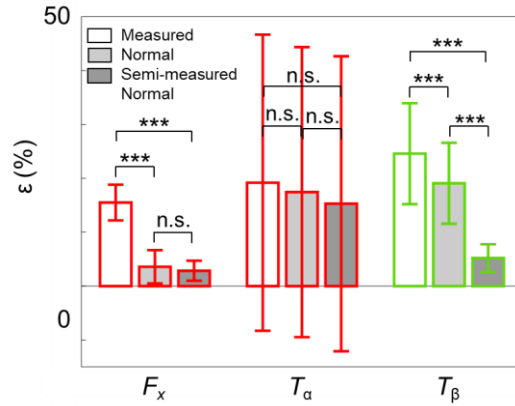


Fig. S1. Relative error ε of using fore-aft force F_x , contact force roll torque T_{α} , and pitch torque T_{β} as the landscape gradients in surface contact cases. White, light gray, and dark gray bars show measured, measured normal, and semi-measured normal forces/torques, separately. Bars and error bars are means ± 1 standard deviation of the average relative error of all average trials. *** $P < 0.001$, n.s.: not significant $P > 0.05$, Student's t-test.

Further studies can try to improve the accuracy of normal direction measurement by designing and manufacturing touch-sensitive cell patterns of smaller resolution and involving vision and other obstacle geometry detection to assist normal direction estimation.

S7. Head oscillation frequency selection

We designed the robot’s head oscillation frequency based on the observed animal behavior (18). When exploring around and negotiating between the beams, the cockroach actively oscillated its head in a changing frequency (**Fig. 6A, B**). To obtain an average oscillation frequency, we separated each head oscillation cycle into two phases—the lowering phase, where the head angle increased, and the raising phase, where the head angle decreased. We defined the amplitude as the maximum range of head angles and angular velocity as the fraction of this amplitude over the time span of each phase. The average amplitude and angular velocity were $15^\circ \pm 9^\circ$ and $145^\circ \pm 100^\circ \cdot \text{s}^{-1}$ in the lowering phases and $16^\circ \pm 10^\circ$ and $150^\circ \pm 90^\circ \cdot \text{s}^{-1}$ in the raising phases for all the observed head oscillation cycles (18). Using these data, we calculated the average head oscillation frequency to be roughly 5 Hz for the animals. Because the animal traversed the beam obstacle in 4 ± 1 seconds (18) while the robot used roughly 10 seconds, the robot head oscillation frequency was designed to be 2 Hz to keep the same head oscillation cycle number.

We also tried two other lower oscillation frequencies, 0.5 Hz and 1 Hz, to test how oscillation frequency affects the conservative force and torque (i.e., landscape gradient) estimation in edge contact cases. We observed for both low head oscillation frequencies ($f = 0.5, 1$ Hz), the estimations were not improved or even worse than without head oscillation ($f = 0$ Hz) ($P < 0.001$, Student’s test) (**Fig. S2**). We speculate that as the head oscillation frequency was low, the relative velocity between the robot and the obstacle at the contact – which decides friction direction – is not governed by the oscillatory motion. So, the frictions from back-and-forth motion did not cancel out each other when averaged temporally. See Section *Why and how head oscillation leads to better landscape gradient estimation* in *Discussion* for explanations.

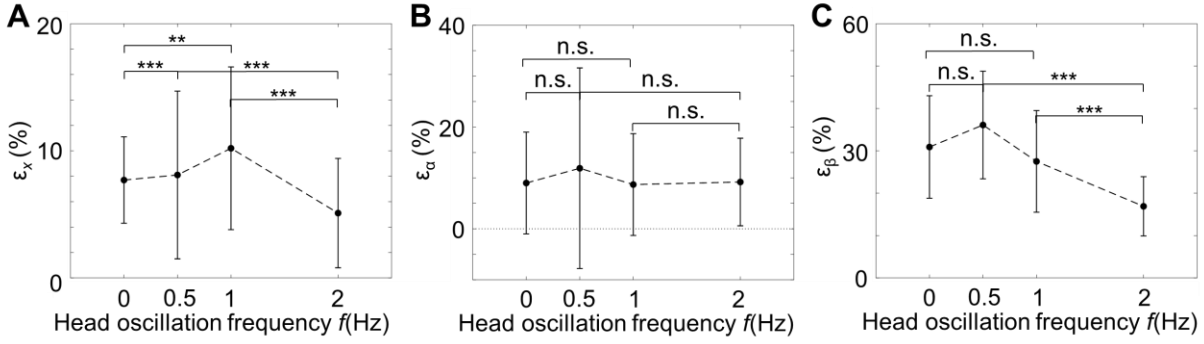


Fig. S2. Relative error of potential energy landscape gradient estimation and landscape reconstruction with various head oscillation frequencies. (A, B, and C) are relative error ϵ_x , ϵ_α , and ϵ_β of using (A) fore-aft force F_x , (B) roll torque T_α , and (C) pitch torque T_β as the landscape gradients, separately. See Section *Comparison criteria and statistics* in *Materials and Methods* for the definition of relative error. Lines and error bars are means \pm 1 standard deviation of the average relative error of all average trials. *** $P < 0.001$, ** $P < 0.01$, n.s.: not significant $P > 0.05$, Student's t-test. Brackets and asterisks show important comparisons described in Section S7.

S8. Various force sensing data observed in repeated experiments

Although our data showed consistency for repeated experiments (x -average coefficient of variation = $2\% \pm 1\%$ for F_x , $2\% \pm 2\%$ for T_α , $3\% \pm 3\%$ for T_β). See how we averaged the repeated trials in Section *Data filtering and averaging* in *Materials and Methods*), we also found that the result was various of some roll and pitch combinations when the head oscillation was involved (maximum coefficient of variation = $20\% \pm 9\%$ for F_x , $24\% \pm 6\%$ for T_α , $27\% \pm 5\%$ for T_β), probably due to the random starting phase of the head oscillation (see Section *Robot experiment protocol* and Section *Data filtering and averaging* in *Materials and Methods*). These trials[†] were mostly (86%) of the roll and pitch combination near the separatrix. We carefully watched the video recording of these trials and speculated that some were caused by head-oscillation-induced pitch-to-roll transition or sudden beam bouncing back.

[†] For $f = 2$ Hz, $\{\alpha, \beta\} = \{35^\circ, 10^\circ\}, \{30^\circ, 20^\circ\}$. For $f = 0.5$ Hz, $\{\alpha, \beta\} = \{35^\circ, 10^\circ\}$. For $f = 1$ Hz, $\{\alpha, \beta\} = \{35^\circ, 10^\circ\}, \{40^\circ, 15^\circ\}, \{40^\circ, 25^\circ\}, \{30^\circ, 20^\circ\}$. See Section S8 for experiments where $f = 0.5$ Hz and 1 Hz.

S9. Successful adapted to sensing and landscape reconstruction strategies to another robot

To test whether our strategies to sense obstacle contact forces and torques to estimate the potential energy landscape gradient and reconstruct the landscape hold for other robots, aside from the shield-shaped robot (**Fig. 3A**), we also designed and built a rounded (i.e., without sharp edge) ellipsoidal robot of the same size (**Fig. S3A, B**), and conducted the same experiment, where it systematically varied roll and pitch angles and was pushed through the beam obstacles without head oscillation ($f = 0\text{Hz}$).

To sense contact forces and torques, the robot was embedded with the same custom 3-D force sensors (**Fig. S3B**, magenta). The pattern of the touch sensory cell distribution was carefully re-designed (**Fig. S3C**) to achieve high sensory accuracy (position resolution $< 11\text{ mm}$, normal direction resolution $< 15^\circ$) (**Fig. S3D**). Especially, because the normal direction changes dramatically around the equator (varying 107° in 50 mm arc length around $z' = 0$), the touch sensory cells were designed to be shortened along z' direction to maintain a small normal direction resolution.

We observed that the measured forces and torques matched conservative ones, with a small relative error of $\varepsilon_x = 12\% \pm 4\%$ in the x direction, $\varepsilon_\alpha = 12\% \pm 11\%$ in the roll direction, and $\varepsilon_\beta = 26\% \pm 10\%$ in the pitch direction. The reconstructed landscape and its gradients matched the ground truth from modeling using the rounded ellipsoidal robot with a low relative error of $\varepsilon_{PE} = 8.6\%$ in potential and $\varepsilon_{Grad} = 13.8\%$ in gradients (**Fig. S3E**). All the estimation errors are roughly equal to or even smaller than that of the shield-shaped robot.

These observations suggested that our obstacle contact force and torque sensing and potential energy landscape reconstruction strategies also adapt to other robot shapes (i.e., universality). Further studies should try to apply these strategies to more robot shapes and obstacle types as verification.

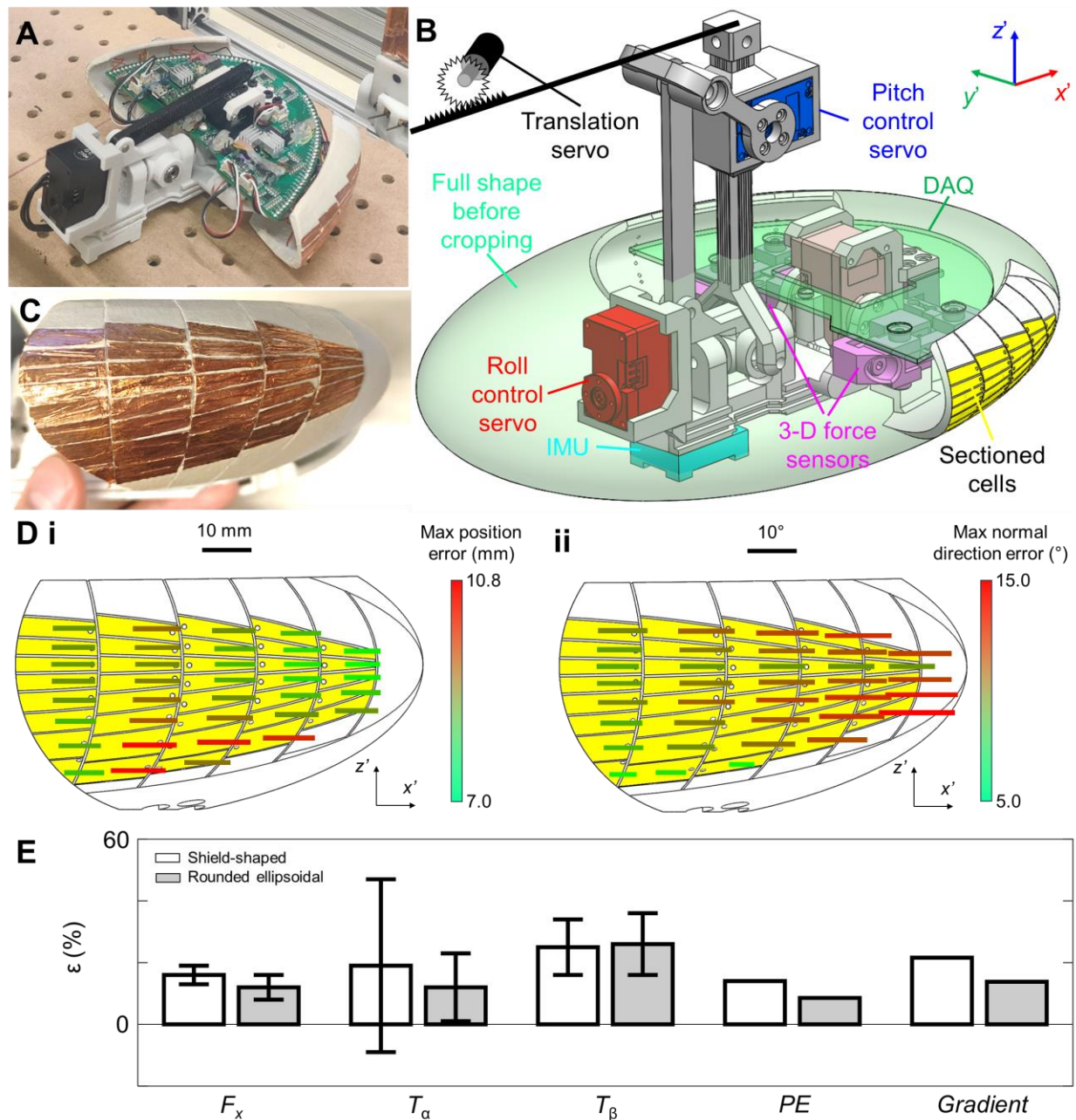


Fig. S3. Same force and torque sensing and landscape reconstruction strategies were applied to a rounded ellipsoidal robot. (A) Photo of the rounded ellipsoidal robot. (B) CAD model of the robot. The robot shell was cropped from a full ellipsoidal shape (translucent green). Other features are the same as in **Fig. 3B**. (C) Touch sensory cells detecting contact positions. The cells were designed to be shortened along z' direction. (D) Maximum (i) position and (ii) normal direction error on each touch-sensitive cell. The pattern of the cell is from robot side view. x' - and z' -axes show robot body frame. Because the left and right

shells are mirrored, only the right shell is presented. Bar rooting at the center of a cell shows error on that cell, whose height and color show error magnitude. (E) Relative error ϵ of using fore-aft force F_x , contact force roll torque T_α , and pitch torque T_β as the landscape gradients, and using reconstructed landscape (PE) and its gradient ($Gradient$) to estimate the ground truth. White and gray bars show using shield-shaped robot (Fig. 3A) and (A) rounded ellipsoidal robot, separately. Bars and error bars are means ± 1 standard deviation of the average relative error of all average trials.

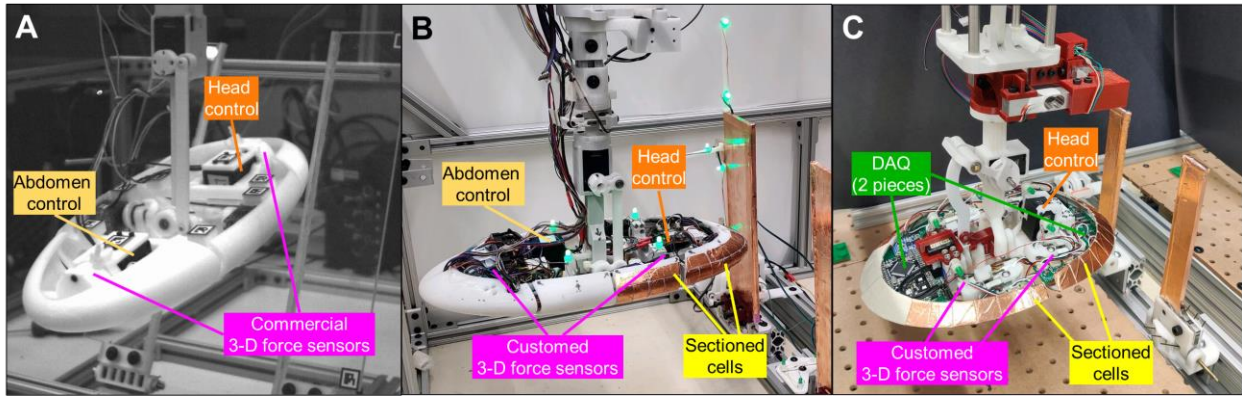


Fig. S4. Iterative development of robots to enable force and contact measurement. (A) The first iteration. The robot was capable of head and abdomen oscillation and contact force sensing using commercial 3-D force sensors. This robot cannot sense the contact position nor separate the contact force with either beam, because the commercial 3-D force sensors were too bulky to place multiple of them in the confined space near the head. (B) The second iteration. Small, low-cost, custom-made 3-D force sensors were used. The head, body, and abdomen were separated from the middle so that the force sensors could individually sense the contact force from either beam. Sectioned cells were planted on the robot’s head and front body surfaces to enable contact position sensing. The robot often suffered from signal loss issues due to the long wiring to a DAQ board that was far from it. (C) The third iteration. To make the robot the same size and shape as in the previous study (9), the body and abdomen were merged, and the shell was designed to be shield-shaped. Custom DAQ boards (2 pieces) were deployed to reduce wiring and signal transmission issues. The robot was damaged once the gap between the head and body was caught by a beam.

Video 1. Robot experiment recording and evolution of reconstructed potential energy landscape. (1 and 2) Video recording of robot experiments (left) and real-time data visualization (right). (1) Head was static. (2) Head was oscillated at 2 Hz. (3) Evolution of reconstructed potential energy landscape (top) as the robot moved forward, compared with ground truth (bottom).

References

1. J. Wessnitzer, B. Webb, Multimodal sensory integration in insects—towards insect brain control architectures. *Bioinspir. Biomim.* **1**, 63–75 (2006).
2. R. Wehner, *Desert Navigator : The Journey of an Ant* (Harvard University Press, Cambridge, MA, 2020).
3. S. J. Sober, P. N. Sabes, Flexible strategies for sensory integration during motor planning. *Nat. Neurosci.* **8**, 490–497 (2005).
4. D. E. Koditschek, What Is Robotics? Why Do We Need It and How Can We Get It? *Annu. Rev. Control. Robot. Autom. Syst.* **4**, 1–33 (2021).
5. E. Rimon, D. E. Koditschek, Exact robot navigation using artificial potential functions. *IEEE Trans. Robot. Autom.* **8**, 501–518 (1992).
6. O. Khatib, Real-Time Obstacle Avoidance for Manipulators and Mobile Robots. *Int. J. Rob. Res.* **5**, 90–98 (1986).
7. J. Tsitsiklis, D. Bertsekas, M. Athans, Distributed asynchronous deterministic and stochastic gradient optimization algorithms. *IEEE Trans. Automat. Contr.* **31**, 803–812 (1986).
8. Boston Dynamics, Spot Autonomous Navigation (2018). https://youtu.be/Ve9kWX_KXus.
9. R. Othayoth, G. Thoms, C. Li, An energy landscape approach to locomotor transitions in complex 3D terrain. *Proc. Natl. Acad. Sci.* **117**, 14987–14995 (2020).

10. R. Othayoth, Q. Xuan, Y. Wang, C. Li, Locomotor transitions in the potential energy landscape-dominated regime. *Proc. R. Soc. B Biol. Sci.* **288**, rspb.2020.2734 (2021).
11. R. R. Murphy, “Disaster robotics” in *Springer Handbook of Robotics*, B. Siciliano, O. Khatib, Eds. (MIT press, 2014).
12. F. Angelini, P. Angelini, C. Angiolini, S. Bagella, F. Bonomo, M. Caccianiga, C. Della Santina, D. Gigante, M. Hutter, T. Nanayakkara, P. Remagnino, D. Torricelli, M. Garabini, Robotic Monitoring of Habitats: The Natural Intelligence Approach. *IEEE Access* **11**, 72575–72591 (2023).
13. C. Li, K. Lewis, The Need for and Feasibility of Alternative Ground Robots to Traverse Sandy and Rocky Extraterrestrial Terrain. *Adv. Intell. Syst.* **5**, 1–8 (2023).
14. C. Li, A. O. Pullin, D. W. Haldane, H. K. Lam, R. S. Fearing, R. J. Full, Terradynamically streamlined shapes in animals and robots enhance traversability through densely cluttered terrain. *Bioinspir. Biomim.* **10**, 046003 (2015).
15. Y. Han, R. Othayoth, Y. Wang, C.-C. Hsu, R. de la Tijera Obert, E. Francois, C. Li, Shape-induced obstacle attraction and repulsion during dynamic locomotion. *Int. J. Rob. Res.* **40**, 939–955 (2021).
16. S. W. Gart, C. Li, Body-terrain interaction affects large bump traversal of insects and legged robots. *Bioinspir. Biomim.* **13**, 026005 (2018).
17. S. W. Gart, C. Yan, R. Othayoth, Z. Ren, C. Li, Dynamic traversal of large gaps by insects and legged robots reveals a template. *Bioinspir. Biomim.* **13**, 026006 (2018).
18. Y. Wang, R. Othayoth, C. Li, Cockroaches adjust body and appendages to traverse cluttered large obstacles. *J. Exp. Biol.* **225** (2022).
19. Q. Xuan, C. Li, Environmental force sensing helps robots traverse cluttered large obstacles.

- Bioinspir. Biomim.* **19**, 016002 (2024).
20. K. Hirai, M. Hirose, Y. Haikawa, T. Takenaka, “The development of Honda humanoid robot” in *Proceedings. 1998 IEEE International Conference on Robotics and Automation (Cat. No.98CH36146)* (IEEE, 1988)vol. 2, pp. 1321–1326.
 21. Qinghua Li, A. Takanishi, I. Kato, “A biped walking robot having a ZMP measurement system using universal force-moment sensors” in *Proceedings IROS '91:IEEE/RSJ International Workshop on Intelligent Robots and Systems '91* (IEEE), pp. 1568–1573.
 22. J. Tan, T. Zhang, E. Coumans, A. Iscen, Y. Bai, D. Hafner, S. Bohez, V. Vanhoucke, “Sim-to-Real: Learning Agile Locomotion For Quadruped Robots” in *Robotics: Science and Systems XIV* (Robotics: Science and Systems Foundation, 2018).
 23. D. Wooden, M. Malchano, K. Blankespoor, A. Howardy, A. A. Rizzi, M. Raibert, “Autonomous navigation for BigDog” in *2010 IEEE International Conference on Robotics and Automation* (IEEE, 2010), pp. 4736–4741.
 24. J. Hwangbo, J. Lee, A. Dosovitskiy, D. Bellicoso, V. Tsounis, V. Koltun, M. Hutter, Learning agile and dynamic motor skills for legged robots. *Sci. Robot.* **4**, 1–14 (2019).
 25. P. Roberts, M. Zadan, C. Majidi, Soft Tactile Sensing Skins for Robotics. *Curr. Robot. Reports* **2**, 343–354 (2021).
 26. S. Sundaram, P. Kellnhofer, Y. Li, J.-Y. Zhu, A. Torralba, W. Matusik, Learning the signatures of the human grasp using a scalable tactile glove. *Nature* **569**, 698–702 (2019).
 27. D. Ramesh, Q. Fu, C. Li, “SenSnake: A snake robot with contact force sensing for studying locomotion in complex 3-D terrain” in *2022 International Conference on Robotics and Automation (ICRA)* (IEEE, 2022), pp. 2068–2075.
 28. G. Yao, L. Xu, X. Cheng, Y. Li, X. Huang, W. Guo, S. Liu, Z. L. Wang, H. Wu, Bioinspired

- Triboelectric Nanogenerators as Self-Powered Electronic Skin for Robotic Tactile Sensing. *Adv. Funct. Mater.* **30**, 1–9 (2020).
29. M. Zhu, M. Lou, I. Abdalla, J. Yu, Z. Li, B. Ding, Highly shape adaptive fiber based electronic skin for sensitive joint motion monitoring and tactile sensing. *Nano Energy* **69**, 104429 (2020).
30. T. Kamegawa, T. Akiyama, Y. Suzuki, T. Kishutani, A. Gofuku, “Three-Dimensional Reflexive Behavior by a Snake Robot with Full Circumference Pressure Sensors” in *2020 IEEE/SICE International Symposium on System Integration (SII)* (IEEE, 2020), pp. 897–902.
31. R. Bajcsy, Y. Aloimonos, J. K. Tsotsos, Revisiting active perception. *Auton. Robots* **42**, 177–196 (2018).
32. F. Qian, D. Goldman, “Anticipatory control using substrate manipulation enables trajectory control of legged locomotion on heterogeneous granular media” in *Micro- and Nanotechnology Sensors, Systems, and Applications VII*, T. George, A. K. Dutta, M. S. Islam, Eds. (2015)vol. 9467, p. 94671U.
33. H. Bhatia, G. Norgard, V. Pascucci, P. T. Bremer, The Helmholtz-Hodge decomposition - A survey. *IEEE Trans. Vis. Comput. Graph.* **19**, 1386–1404 (2013).
34. D. Biswas, A. Lamperski, Y. Yang, K. Hoffman, J. Guckenheimer, E. S. Fortune, N. J. Cowan, Mode switching in organisms for solving explore-versus-exploit problems. *Nat. Mach. Intell.*, doi: 10.1038/s42256-023-00745-y (2023).
35. J. C. Tuthill, R. I. Wilson, Mechanosensation and Adaptive Motor Control in Insects. *Curr. Biol.* **26**, R1022–R1038 (2016).
36. J. Mi, Y. Wang, C. Li, “Omni-Roach: A Legged Robot Capable of Traversing Multiple Types of Large Obstacles and Self-Righting” in *2022 International Conference on Robotics and Automation (ICRA)* (IEEE, 2022), pp. 235–242.

37. G. Cybenko, Approximation by superpositions of a sigmoidal function. *Math. Control. Signals, Syst.* **2**, 303–314 (1989).
38. K. Hornik, M. Stinchcombe, H. White, Multilayer feedforward networks are universal approximators. *Neural Networks* **2**, 359–366 (1989).
39. C. M. Bishop, *Pattern Recognition and Machine Learning* (springer, New York, 2006).
40. J. Okada, Y. Toh, The role of antennal hair plates in object-guided tactile orientation of the cockroach (*Periplaneta americana*). *J. Comp. Physiol. A Sensory, Neural, Behav. Physiol.* **186**, 849–857 (2000).
41. T. J. Prescott, M. E. Diamond, A. M. Wing, Active touch sensing. *Philos. Trans. R. Soc. B Biol. Sci.* **366**, 2989–2995 (2011).
42. D. Biswas, L. A. Arend, S. A. Stamper, B. P. Vágvölgyi, E. S. Fortune, N. J. Cowan, Closed-Loop Control of Active Sensing Movements Regulates Sensory Slip. *Curr. Biol.* **28**, 4029-4036.e4 (2018).
43. Y. Baba, A. Tsukada, C. M. Comer, Collision avoidance by running insects: antennal guidance in cockroaches. *J. Exp. Biol.* **213**, 2294–2302 (2010).
44. J. Okada, Y. Toh, Active tactile sensing for localization of objects by the cockroach antenna. *J. Comp. Physiol. A* **192**, 715–726 (2006).
45. C. Schütz, V. Dürr, Active tactile exploration for adaptive locomotion in the stick insect. *Philos. Trans. R. Soc. B Biol. Sci.* **366**, 2996–3005 (2011).
46. V. Berendes, V. Dürr, Active tactile exploration and tactually induced turning in tethered walking stick insects. *J. Exp. Biol.* **225** (2022).
47. R. Othayoth, B. Strebel, Y. Han, E. Francois, C. Li, A terrain treadmill to study animal locomotion

- through large obstacles. *J. Exp. Biol.* **225** (2022).
48. M. J. Hartmann, Active sensing capabilities of the rat whisker system. *Auton. Robots* **11**, 249–254 (2001).
 49. N. O. Zweifel, M. J. Z. Hartmann, Defining “active sensing” through an analysis of sensing energetics: homeoactive and alloactive sensing. *J. Neurophysiol.* **124**, 40–48 (2020).
 50. N. E. Bush, S. A. Solla, M. J. Hartmann, Whisking mechanics and active sensing. *Curr. Opin. Neurobiol.* **40**, 178–188 (2016).
 51. M. J. Z. Hartmann, A night in the life of a rat: Vibrissal mechanics and tactile exploration. *Ann. N. Y. Acad. Sci.* **1225**, 110–118 (2011).
 52. A. E. Schultz, J. H. Solomon, M. A. Peshkin, M. J. Hartmann, Multifunctional whisker arrays for distance detection, terrain mapping, and object feature extraction. *Proc. - IEEE Int. Conf. Robot. Autom.* **2005**, 2588–2593 (2005).
 53. J. H. Solomon, M. J. Z. Hartmann, Extracting object contours with the sweep of a robotic whisker using torque information. *Int. J. Rob. Res.* **29**, 1233–1245 (2010).
 54. H. M. Emmett, M. M. Graff, M. J. Z. Hartmann, A Novel Whisker Sensor Used for 3D Contact Point Determination and Contour Extraction. *Robot. Sci. Syst.*, doi: 10.15607/RSS.2018.XIV.059 (2018).
 55. L. A. Huet, J. W. Rudnicki, M. J. Z. Hartmann, Tactile sensing with whiskers of various shapes: Determining the three-dimensional location of object contact based on mechanical signals at the whisker base. *Soft Robot.* **4**, 88–102 (2017).
 56. L. A. Huet, H. M. Emmett, M. J. Z. Hartmann, Demonstration of three-dimensional contact point determination and contour reconstruction during active whisking behavior of an awake rat. *PLoS Comput. Biol.* **18**, 1–28 (2022).

57. W. J. Bell, L. M. Roth, C. A. Nalepa., *Cockroaches: Ecology, Behavior, and Natural History* (John Hopkins University Press, Baltimore, MD, 2007).
58. H.-U. Thiele, *Carabid Beetles in Their Environments: A Study on Habitat Selection by Adaptations in Physiology and Behaviour* (Springer Science & Business Media, Berlin, Heidelberg, New York, 1977).
59. J. C. Tuthill, E. Azim, Proprioception. *Curr. Biol.* **28**, R194–R203 (2018).
60. J. C. Tuthill, R. I. Wilson, Mechanosensation and Adaptive Motor Control in Insects. *Curr. Biol.* **26**, R1022–R1038 (2016).
61. H. B. Schlegel, Following gradient extremal paths. *Theor. Chim. Acta* **83**, 15–20 (1992).
62. C. M. Smith, How to find a saddle point. *Int. J. Quantum Chem.* **37**, 773–783 (1990).
63. G. Henkelman, G. Jóhannesson, H. Jónsson, “Methods for Finding Saddle Points and Minimum Energy Paths” in *Theoretical Methods in Condensed Phase Chemistry* (Kluwer Academic Publishers, Dordrecht, 2008), pp. 269–302.
64. J. M. Bello-Rivas, A. Georgiou, H. Vandecasteele, I. G. Kevrekidis, Gentlest Ascent Dynamics on Manifolds Defined by Adaptively Sampled Point-Clouds. *J. Phys. Chem. B* **127**, 5178–5189 (2023).
65. L. Zhang, W. Ren, A. Samanta, Q. Du, Recent developments in computational modelling of nucleation in phase transformations. *npj Comput. Mater.* **2**, 16003 (2016).
66. W. Quapp, M. Hirsch, O. Imig, D. Heidrich, Searching for saddle points of potential energy surfaces by following a reduced gradient. *J. Comput. Chem.* **19**, 1087 (1998).
67. J. M. Bello-Rivas, A. Georgiou, J. Guckenheimer, I. G. Kevrekidis, Staying the course: iteratively locating equilibria of dynamical systems on Riemannian manifolds defined by point-clouds. *J.*

- Math. Chem.* **61**, 600–629 (2023).
68. Y. Xian, C. H. Lampert, B. Schiele, Z. Akata, Zero-Shot Learning—A Comprehensive Evaluation of the Good, the Bad and the Ugly. *IEEE Trans. Pattern Anal. Mach. Intell.* **41**, 2251–2265 (2019).
69. R. W. Pastor, “Techniques and Applications of Langevin Dynamics Simulations” in *The Molecular Dynamics of Liquid Crystals* (Springer Netherlands, Dordrecht, 1994), pp. 85–138.
70. M. I. Jordan, “Dynamical, symplectic and stochastic perspectives on gradient-based optimization” in *Proceedings of the International Congress of Mathematicians (ICM 2018)* (WORLD SCIENTIFIC, 2019)vol. 1, pp. 523–549.
71. X. Cheng, D. Yin, P. L. Bartlett, M. I. Jordan, Stochastic Gradient and Langevin Processes. *37th Int. Conf. Mach. Learn. ICML 2020 PartF16814*, 1788–1797 (2019).
72. S. Li, B. Dutta, S. Cannon, J. J. Daymude, R. Avinery, E. Aydin, A. W. Richa, D. I. Goldman, D. Randall, Programming active cohesive granular matter with mechanically induced phase changes. *Sci. Adv.* **7**, 1–12 (2021).
73. R. Othayoth, C. Li, Propelling and perturbing appendages together facilitate strenuous ground self-righting. *eLife* **10**, 1–23 (2021).
74. C. Li, Recent progress in the physical principles of dynamic ground self-righting. (2024).
75. G. Patane, Meshless Approximation and Helmholtz-Hodge Decomposition of Vector Fields. *IEEE Trans. Vis. Comput. Graph.* **28**, 1–14 (2022).
76. F. H. Razafindrazaka, K. Poelke, K. Polthier, L. Goubergrits, A Consistent Discrete 3D Hodge-type Decomposition: implementation and practical evaluation. (2019).
77. A. Lemoine, J. P. Caltagirone, M. Azañez, S. Vincent, Discrete Helmholtz–Hodge Decomposition

- on Polyhedral Meshes Using Compatible Discrete Operators. *J. Sci. Comput.* **65**, 34–53 (2015).
78. E. Deriaz, V. Perrier, Divergence-free and curl-free wavelets in two dimensions and three dimensions: Application to turbulent flows. *J. Turbul.* **7**, 1–37 (2006).
79. Q. Guo, M. K. Mandal, M. Y. Li, Efficient Hodge-Helmholtz decomposition of motion fields. *Pattern Recognit. Lett.* **26**, 493–501 (2005).
80. D. Q. Nguyen, R. Fedkiw, H. W. Jensen, Physically based modeling and animation of fire. *Proc. 29th Annu. Conf. Comput. Graph. Interact. Tech. SIGGRAPH '02*, 721–728 (2002).